DOE/BC/14600-41
Distribution Category UC-122

Aspects of Non-Newtonian Flow and Displacement in Porous Media

DOE/BC/14600--41

DE93 000128

Topical Report

By
Charul Shah
Yanis C. Yortsos

February 1993

Work Performed Under Contract No. DE-FG22-90BC14600

Prepared for
U.S. Department of Energy
Assistant Secretary for Fossil Energy

Thomas B. Reid, Project Manager
Bartlesville Project Office
P.O. Box 1398
Bartlesville, OK 74005

Prepared by
University of Southern California
Petroleum Engineering Program
Department of Chemical Engineering
Los Angeles, CA 90089-1211

Contents

List of Figures

1 INTRODUCTION

The flow of fluids through a variety of porous media is common in many petroleum engineering applications. A partial list includes filtration, ground water flow, production of oil and gas from underground reservoirs, ion exchange and adsorption [12, 42]. Most of these involve either single- or multi-phase flow of fluids in order to achieve desired objectives. In some of these applications, non-Newtonian fluids are extensively involved. Particular examples include heavy oils and Enhanced Oil Recovery (EOR). The rheology of many heavy oils has been shown to be non-Newtonian, Bingham plastics being one manifestation of heavy oil flow. In EOR applications, non-Newtonian fluids such as low concentration polymer solutions, emulsions, gels etc. are simultaneously injected to increase the viscosity of driving agents that displace oil. Such rheologically complex fluids are used to improve sweep efficiencies, divert displacing fluids and block swept zones.

While the flow of Newtonian fluids through porous media has been well understood through a variety of experimental and theoretical techniques, the state of the art in the flow of non-Newtonian fluids, either single- or multiphase, in porous media is far from complete. Reasons for this include the complex rheological behavior in combination with the complicated flow geometry of porous media. The macroscopic description for the flow of non-Newtonian fluid through porous media is therefore a difficult task [37, 44]. With few exceptions, laws equivalent to Darcy's law for the flow of non-Newtonian fluids through porous media have not been developed.

The present study has been undertaken to understand the flow of non-Newtonian fluids through porous media. The work considered involves the numerical (pore network) modeling of both single- and multiphase flow of power-law and Bingham plastic fluids in network-like porous media. We consider aspects of both single- and multi-phase flow and displacement. Section 2 describes elementary aspects of non-Newtonian flow and some simple models for porous media. Viscoelastic effects in the flow of non-Newtonian fluids are also discussed. The section includes a brief literature review on non-Newtonian flow in porous media. Section 3 describes single-phase flow. It is shown that the critical path approach of Ketz and Thompson [21] as extended by Yortsos [53] is well suited for power-law fluids except for very small values of the power-law index n. The numerical simulation of the single-phase flow of both shear thinning and shear thickening fluids is also presented. The single-phase flow of a Bingham plastic type fluid is simulated in Section 4. Section 5 deals with the immiscible displacement of a Newtonian fluid by a non-Newtonian fluid both for constant pressure

and constant rate boundary conditions. Finally, Section 6 considers drainage of a power-law fluid by another power-law fluid of the same power-law index but of different consistency index. An appropriate phase diagram is constructed for this case.

2 RHEOLOGICAL AND POROUS MEDIA ASPECTS

We begin with a brief review of relevant rheological and porous media aspects useful to the subsequent analysis.

2.1 SIMPLE MODELS FOR NON-NEWTONIAN FLUIDS

In non-Newtonian fluids, the viscosity is shear rate dependent. Various empirical, rheological models have been used to characterize such behavior. For simple shear flow, the relation between shear stress (τ) and shear rate ($\dot{\gamma}$) is expressed as [3]

$$\tau = -\eta\dot{\gamma} \tag{1}$$

where η is a function of the shear rate. Figure 1 sketches schematically this behavior. When the viscosity decreases with increasing shear rate under steady shear flow, the fluid is shear thinning or pseudoplastic (curve D), in the opposite case the fluid is shear thickening or dilatant (curve C). Some fluids may behave as a solid (shown by curves B and E) and will not flow until a critical yield stress is exceeded (viscoplastic). Many heavy oils are reported to exhibit such behavior. Various empirical equations have been proposed to describe steady state flow of non-Newtonian fluids. Four representative models widely used for inelastic fluids are discussed below.

Power-law (Ostwald-de- Waele) fluids are two-parameter models represented by

$$\tau = -K\dot{\gamma}^n \tag{2}$$

hence

$$\eta = K\dot{\gamma}^{n-1} \tag{3}$$

where K is a consistency index and the difference between n and unity indicates the degree of departure from Newtonian behavior. The fluid is shear thinning for $n < 1$ and shear thickening for

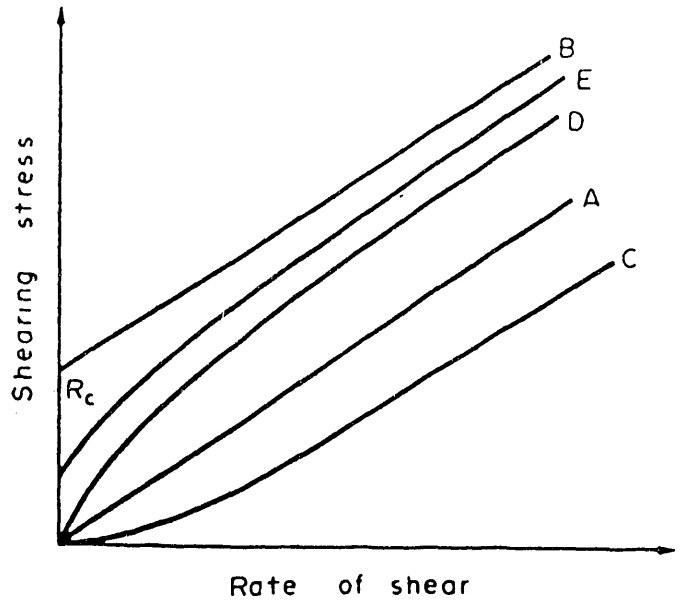

Figure 1: Classification of Non-Newtonian Fluids Based on Shear Stress-Shear Rate Behavior.

$n > 1$. For n=1, the model reduces to Newtonian, where $K = \mu$. This model gives an adequate description of fluid behavior over an intermediate range of shear rates although it fails to describe the limiting viscosities at zero or at infinite shear rates. Power-law models were extensively used in non-Newtonian studies by Christopher and Middleman [10], Marshall and Metzner [27], Teeuw and Hesslink [47], Savins [38], Willhite and Uhl [50] and Cannella and Huh [7].

Ellis models are represented by the expression

$$\frac{1}{\eta} = \frac{1}{\eta_o}[1 + (\frac{|\tau|}{\tau_{1/2}})^{\alpha-1}] \tag{4}$$

hence

$$\dot{\gamma} = \frac{\tau}{\eta_o}[1 + (\frac{|\tau|}{\tau_{1/2}})^{\alpha-1}] \tag{5}$$

where η_o, $\tau_{1/2}$ and α are fluid parameters. η_o is the zero shear rate viscosity, while $\tau_{1/2}$ is the value of the shear stress for which the corresponding viscosity is equal to one-half its value at zero shear rate. This three-parameter model is extremely flexible and includes Newtonian and power-law behaviors as special cases. Sadowski and Bird [34] used the Ellis models to describe the

shear-sensitive viscosities of various fluids. Based on their theoretical analysis, Duda et al. [14] recommended Ellis models for the study of inelastic non-Newtonian flow.

Another quite useful model was proposed by Carreau [8] and it is expressed as

$$\tau = \eta_\infty + (\eta_o - \eta_\infty)(1 + \lambda\dot{\gamma}^2)^{\frac{n-1}{2}}\dot{\gamma} \tag{6}$$

hence

$$\eta = \eta_\infty + (\eta_o - \eta_\infty)(1 + \lambda\dot{\gamma}^2)^{\frac{n-1}{2}} \tag{7}$$

where η_o is as defined above, while η_∞ describes the limiting viscosity at infinite shear rate. The time constant λ is a measure of the transition between the lower Newtonian and shear thinning region and n is the power-law index. Recently, Sorbie et al. [44] have used this model for the numerical simulation of shear thinning fluids in porous media.

Finally, Bingham plastic type fluids follow a two-parameter model such that

$$\text{if} \quad |\tau| < \tau_o, \ \tau = \tau_o - \mu_o\dot{\gamma} \tag{8}$$

and

$$\text{if} \quad |\tau| < \tau_o, \ \dot{\gamma} = 0 \tag{9}$$

τ_o is the yield stress that must be exceeded for flow to begin, while μ_o is the Bingham plastic coefficient. Such fluids remain rigid when the value of shear stress is smaller than τ_o, but flow like Newtonian fluids when the shear stress exceeds τ_o.

2.2 VISCOELASTIC EFFECTS

Many shear thinning fluids used in EOR applications exhibit elastic characteristics. Such fluids do exhibit shear thinning but in addition they also display extensional viscosity effects. In our subsequent analysis, we have neglected such issues. Complications, however, are certain to arise when the pressure drop in porous media is large enough for extensional viscosity effects to be important [19]. Jones and Walters [19, 20] have reported that above a critical set of conditions a significant increase in the flow resistance in a porous media is observed. This has been attributed

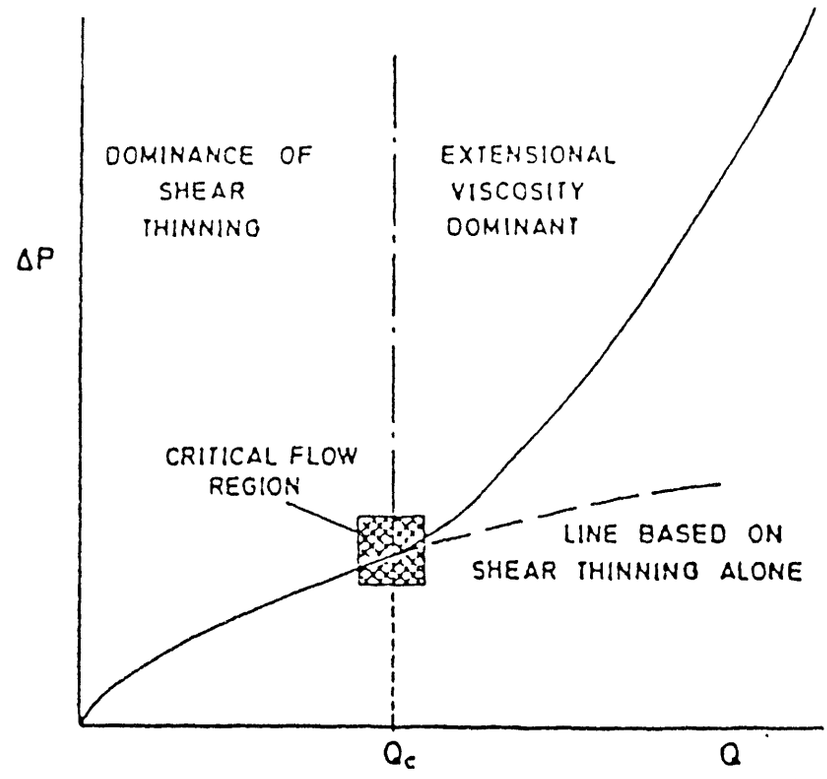

Figure 2: Typical Flow Behavior of Viscoelastic Fluids in Porous Media (from [19]).

to the high extensional viscosities found in dilute polymer solutions at moderate to high strain rates. It is obvious that extensional viscosity would be important near the wellbore, where strain rates are the highest. Moreover, extensional viscosity becomes important whenever the flow of non-Newtonian fluids occurs through geometries such that the cross sectional area is not uniform. This section summarizes the pertinent literature on the subject.

The converging-diverging geometries of porous media may contribute to the overall pressure drop due to the generation of extensional flow. Jones and Walters [19] studied both extensional as well as shear flows for the determination of the rheological properties of very dilute aqueous solutions of Xanthan Gum and Polyacrylamide, both of which are of potential use in EOR. For polyacrylamide solution, a critical strain rate region was identified, beyond which extensional viscosity effects are likely to be important in practical polymer flooding. Figure 2 shows the general flow behavior of viscoelastic fluids in geometries which can induce extensional viscosity effects. Critical flow rates between 0.02 to 0.4 cc/sec were reported based on the type of geometries shown in Figure 3. The corresponding Reynolds numbers are quite low and range between 0.04 to 0.06. In contrast, Xanthan Gum solution, which is both shear thinning and tension thinning, has an extensional viscosity behavior different from that of the high molecular weight polyacrylamide.

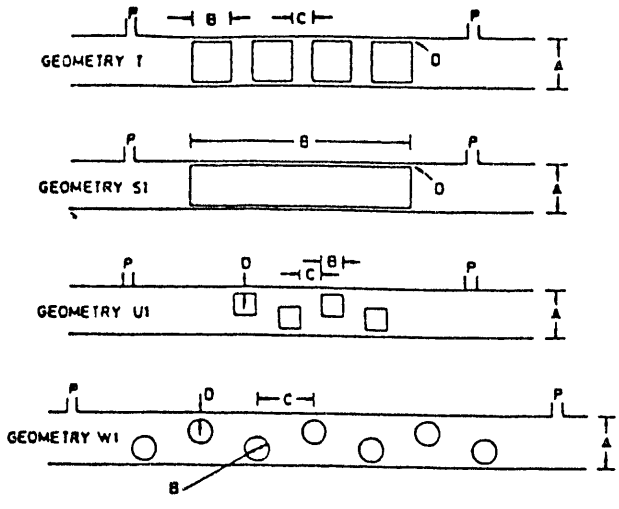

Geometry	A	B	C	D
U1	25	12.5	12.5	3
W1	23	12.5	33.75	2.5

Geometry	A	B	C	D
T1	28	24.5	12.5	1.45
T2	13.5	12.5	6.75	0.75
T3	6.2	5.9	3.2	0.4
S1	28	137	-	1.4

Dimensions of model geometries

Figure 3: Typical Model Geometries (from [19])

In examining the flow of non-Newtonian elastic fluids, Boger [6] pointed out that vortex enhancement is linked with an increased pressure loss through the contraction region. Binding and Walters [2] carried out a study to measure pressure drops in contraction flow geometries for the determination of the extensional behavior of polymer solutions. The flow rates used during their study were in the range of $10^{-7} - 10^{-4} m^3/s$. They reported that Boger fluids (which are highly-elastic, constant-viscosity, non-Newtonian fluids) displayed vortex enhancement in axisymmetrical, but not in planner contractions, while aqueous solutions of polyacrylamide exhibited vortex enhancement in both geometries. On the other hand, Evans and Walter [16] carried out experiments with a wide variety of geometries to examine the flow of aqueous polyacrylamide solutions and reported that the flow characteristics in contraction flows are difficult to generalize from one type of contraction to another. Durst [15] studied porous media flows of dilute polymer solutions and showed that the small addition of high molecular weight polymers to a Newtonian solvent triggers pressure drops if the flow rate exceeds an onset flow rate corresponding to a critical Deborah number for the porous media-polymer solution matrix. The critical Deborah number was identified as 0.5.

Another important viscoelastic effect identified is the Trouton ratio, given by [19, 20]

$$T_R = \frac{\eta_E(\dot{\varepsilon})}{\eta(\dot{\gamma})} \tag{10}$$

where η_E is the extensional viscosity based on the strain rate $\dot{\varepsilon}$ and η is the shear viscosity at the shear rate $\dot{\gamma}$. For Newtonian fluids, the Trouton ratio is constant ($T_R = 3$), whereas highly elastic fluids have high T_R. Jones et al. [20] reported that the Trouton ratio increases with an increase in the strain rate, both for a Boger fluid and for an aqueous solutions of polyacrylamide at constant shear viscosity.

2.3 MODELS FOR POROUS MEDIA FLOW

Important properties of natural porous media are heterogeneity, correlation structures, geometry and topology of the pore space and pore size distribution [13]. Early approaches to model flow in porous media relied on simple geometric models, where the geometry of the porous media is greatly simplified to allow for the governing differential equations to be solved [48]. A most commonly used model in the early literature is the bundle of capillary tubes where porous media is modelled as a set of parallel capillaries with distributed sizes. A skewed capillary model, which is a minor variation of the well-known straight capillary model, has also been reported [48].

Recent approaches to model porous media involve networks of capillaries [24, 45]. In this approach, the porous media is a network of bonds (shown schematically in Figure 4). Individual pores have defined geometrical properties (typically cylinders of constant diameter) with different pores having different size characteristics. The bonds are connected to each other at sites or nodes of different size. The average number of connections at a site is the coordination number z of the network. Most commonly used network models are square lattices with coordination number 4 (in 2-D) and cubic lattice with coordination number 6 (in 3-D).

The majority of work on single-phase flow of non-Newtonian fluids through porous media (restricted mainly to polymer solutions) is based on the capillary tube bundle model for porous media and some suitable rheological models for the non-Newtonian fluid. Power-law, Ellis and Correau models have been extensively used for such studies. A comprehensive review on this subject is presented by Savins [39]. An important aspect of the flow of non-Newtonian fluids in porous media is the interaction between fluid and porous media in terms of plugging, adsorption, chemical reaction etc. Salman [36] recently has presented an excellent review of this aspect.

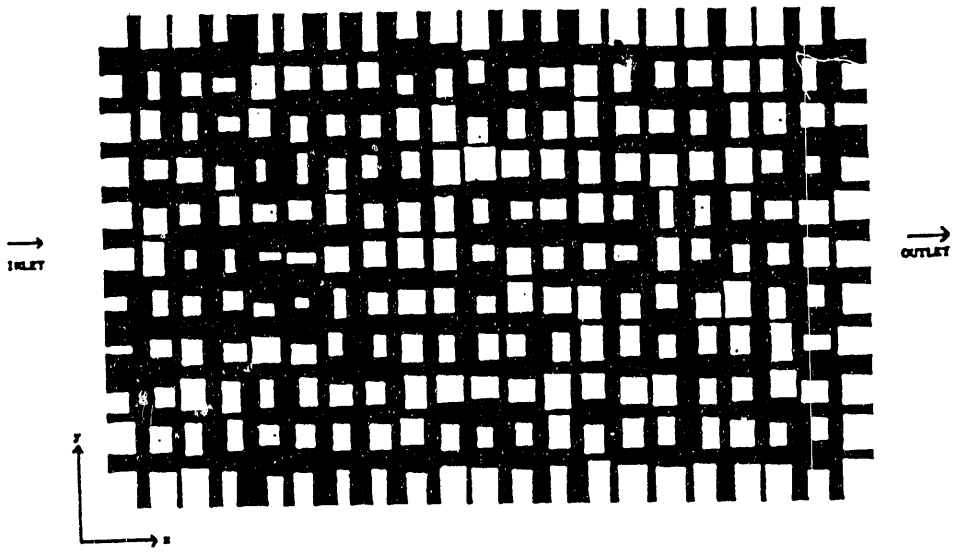

Figure 4: Typical Network Model.

Bird et al. [3] were the first to suggest the scale up of rheologically complex fluid flow in porous media based on the capillary model, with an assumed functional relationship between shear stress and shear rate. Their equation for power-law fluids is

$$u^n = (k/H)|\bigtriangledown P| \tag{11}$$

where

$$H = K[2(\frac{25}{12})^n(\frac{3n+1}{n})^n(3)^{n+1}/150][D_p]^{1-n}[\phi]^{2(n-1)} \tag{12}$$

u denotes superficial velocity, D_p is the mean particle diameter of porous media, n is the power-law index, K is the consistency index, ϕ is the porosity of porous media and k the absolute permeability. Christopher and Middleman [10] modified the Blake-Kozeny equation for purely viscous fluids. Their equation for a power law fluid may be summarized as follows

$$u^n = (k/H)\Delta P/L \tag{13}$$

where

$$H = \frac{K}{12}(\frac{9n+3}{n})^n(150k\phi)^{\frac{(1-n)}{2}} \tag{14}$$

Teeuw and Hesselink [47] accounted for effects of tortuosity on both shear rate and shear stress by considering

$$u = (\frac{\phi n}{3n+1})(\frac{8k}{\phi})^{\frac{(n+1)}{2n}}(\frac{\Delta P}{2KL})^{1/n} \tag{15}$$

Sadowski [35, 34] employed the same capillary model to represent porous media, but used an Ellis model for the fluid. The flow equation may be expressed as

$$u = (k/H)\Delta P/L \tag{16}$$

where

$$\frac{1}{H} = \frac{1}{\mu^o}[1 + (4/((2n+1)/n))(\frac{\tau_{RH}^{\frac{1-n}{n}}}{\tau_{1/2}})] \tag{17}$$

where τ_{RH} is

$$\tau_{RH} = [\phi D_p/6(1-\phi)]\Delta P/L \tag{18}$$

The single-phase flow of Xanthan biopolymers through porous media has been studied by Hirasaki and Pope [18], Greaves and Patel [17], Whillhite and Uhl [50] and Chaveteau and coworkers [9, 54], all with the use of power-law models. A detailed review on these works has been presented recently by Sorbie [46].

Duda et al. [14] and Sheffield and Metzner [42] have reported the inadequacy of conventional capillary model for the description of the flow of nonlinear but purely viscous fluids through porous media. They mentioned that this adequacy may lead to order-of-magnitude error in pressure drop-flow rate predictions. Duda et al. [14] concluded that models for porous media must also include expansion and contraction geometry, while rheological models for the fluid must include the characteristic transition from Newtonian behavior at low shear rate to shear thinning behavior at high shear rate.

Cannella and Huh [7] have recently investigated the flow behavior of Xanthan biopolymer in porous media both experimentally and theoretically. They applied a power-law rheological model

for Xanthan solutions and derived a relation for the apparent viscosity in porous media based on a qualitative argument by employing the effective medium approximation. This was the first approach where porous media were modelled as a network of capillaries. Sorbie et al. [44] have also recently used network models to relate the behavior of single-phase flow of a Carreau fluid in a single capillary and at the macroscopic scale.

2.4 MULTIPHASE FLOW OF NON-NEWTONIAN FLUIDS THROUGH POROUS MEDIA

The literature is comprehensive on the subject of multiphase flow of Newtonian fluids through porous media. Lenormand et al. [25, 26] presented a study on drainage flow patterns where a Newtonian fluid displaces another Newtonian fluid. In their numerical study, they have employed network models and presented computer simulations of immiscible displacement. They have characterized immiscible displacement in porous media by two dimensionless numbers, the capillary number Ca, which is the ratio of viscous forces to capillary forces, and the ratio of the two viscosities M. Depending on the values of Ca and M three types of displacement patterns have been identified: viscous fingering, capillary fingering and stable displacement. Lenormand identified the boundaries of each domain (Figure 5) and described the three regions by simple statistical models, such as percolation [49], DLA and anti-DLA [32], for capillary fingering, viscous fingering and compact displacements, respectively. He also showed how these boundaries scale with the model size, a significant result for scale up processes.

On the contrary, very little research is reported on multiphase flow, where one or more fluids are non-Newtonian in nature. Immiscible displacement of a Newtonian fluid by a non-Newtonian fluid occurs in many processes which involve non-Newtonian fluids, such as polymer or foam. However, there is a severe lack of understanding of such displacements. Slattery [43] was the first to extend local averaging to multiphase flow of viscoelastic liquids in porous media. Schneider and Owens [40] conducted steady state measurements of relative permeability for polymer-oil systems. Savins et al. [39] recently carried out oil flood experiments in porous media, involving a non-Newtonian displacing phase and a Newtonian displaced phase. They have developed a model to interpret purely viscous rheological behavior in multiphase flow by considering a capillary model for porous media and an empirical power-law model for non-Newtonian rheology. More recently, Salman [36] reported

an experimental study using kerosene and different polymer solutions on Berea sandstone cores. Salman et al. [37] modified the Buckley-Leverett theory for power-law fluids and the JBN method to calculate individual relative permeabilities in multiphase system for power-law fluids. Witherspoon et al. [51] also reported displacement of a Bingham non-Newtonian fluid by a Newtonian fluid to obtain insight in the physics of two-phase displacement. However, their approach is mostly phenomenological.

In a series of articles, Pascal [28, 29, 30, 31] reported on the macroscopic interface stability involving non-Newtonian fluids. He described the conditions under which piston-like displacement can be obtained, when one or both fluids are of the power-law type. The stability condition with a non-Newtonian displacing fluid of a power-law type is

$$\frac{\mu_2}{\mu_{eff}} V^{1-n} < 1 \tag{19}$$

where μ_2 and μ_{eff} denote viscosity of the displaced phase and effective viscosity of the non-Newtonian displacing fluid, respectively, while V is the interface velocity. This result is different from its Newtonian counterpart, where no velocity dependence exists (n=1).

So far all theoretical-numerical studies for displacement involving non-Newtonian fluids are restricted to the macroscopic scale, where various phenomenological models, mostly extensions of Newtonian behavior, have been used. To the best of our knowledge, there is no study reported in the literature on the multiphase flow of rheologically complex fluids where a network model has been employed. This study is undertaken in this report.

3 SINGLE-PHASE FLOW OF POWER-LAW FLUIDS IN POROUS MEDIA

The objective of this section is to understand the flow patterns in single-phase flow of power-law fluids for different model parameters assuming power-law behavior in the pores of the network. For simulation purposes we have used a network model as also done by Sorbie et al. [44]. The following assumptions are made:

(i) All bonds in the network are of uniform cross-section, so that any contribution due to converging-diverging geometries to the pressure drop is not significant. Hence, the overall pressure

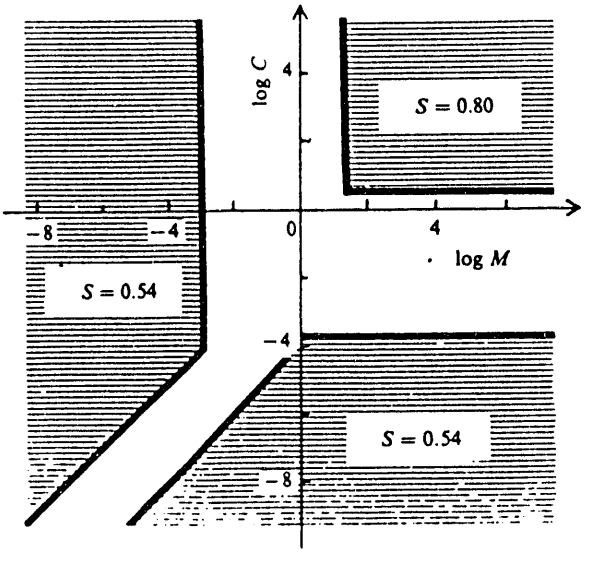

Figure 5: Immiscible Displacement Phase Diagram.

drop in the capillary is related to the average flow rate by a power-law

$$q = g(\Delta P)^{1/n} \tag{20}$$

where q is the volume flow rate in a pore of conductance g, across which there is an applied pressure drop ΔP. This assumption ignores pressure drops associated with extensional flow and converging-diverging geometries. Hence, the model inherently predicts a macroscopic power-law exponent equal to the one at the pore level.

(ii) Although there is a considerable experimental evidence of adsorption on the porous media surface, which thereby reduce the mobility of the flowing phase [11], we have neglected such surface effects for simplicity.

(iii) The fluids considered are inelastic. This is true for the widely used polymers xanthan gum, although not for polyacrylamide solutions which exhibit shear thinning as well as elastic behavior under certain conditions. Heavy oils also exhibit some viscoelasticity [22]. However, our scope is to first understand shear thinning and shear thickening behavior of simpler fluids such as power-law.

Under the above qualifications, which render the problem to one of power-law resistors, the following aspects have been addressed: (i) Application of Effective Medium Theory and (ii) Ap-

plication of the Critical Path Analysis. Both issues are briefly discussed theoretically before their validity is tested by the use of numerical simulation.

3.1 EFFECTIVE MEDIUM THEORY

Effective Medium Theory (EMT) is an important technique that has been used to interpret the flow of non-Newtonian fluids in porous media [46]. It was originally developed to estimate the effective electrical conductivity for a regular linear network with randomly distributed conductivities [23]. If g is the conductivity of a resistor and $G(g)$ its normalized probability distribution, the effective conductivity g_m can be obtained from the expression

$$\int_0^\infty \frac{(g_m - g)}{[g + (z/2 - 1)g_m]} G(g)dg = 0 \tag{21}$$

where z is the coordination number for the network. This equation has been successfully used for calculating certain average properties for Newtonian fluids using network models. Cannella and Huh [7] have recently used mainly qualitative arguments to propose the following expression for g_m

$$\int_0^\infty G(g)[(\frac{zg_m/2}{g + (z/2 - 1)g_m})^n - 1]dg = 0 \tag{22}$$

for flow involving power-law fluids. In a different approach, Yortsos [53] applied EMT theory to Bethe lattices at large coordination numbers. As shown in Figure 6, such a lattice lacks interconnections, hence it is most suitable for analytical calculations, and it has often been used for porous media applications. Yortsos [53] derived the following EMT

$$\int_0^\infty G(g)[\frac{(z-1)g}{(g^n + ((z-1)^n - 1)g_m^n)^{1/n}} - 1]dg = 0 \tag{23}$$

from the solution of which the average and total conductances $<g>$ and $<g_T>$, respectively, can be evaluated

$$< g >= ((z-1)^n - 1)^{1/n} g_m \tag{24}$$

$$< g_T >= \frac{z}{z-1} < g > \tag{25}$$

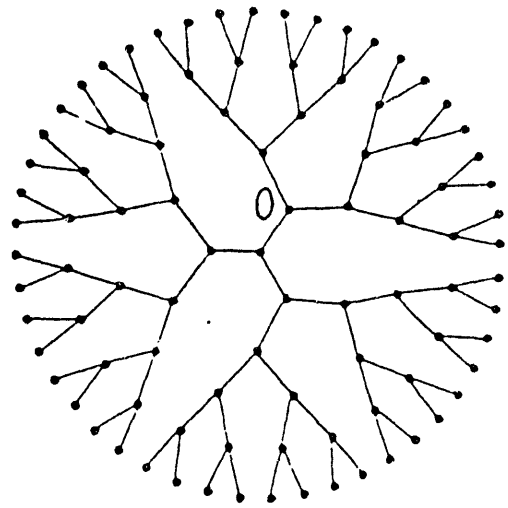

Figure 6: Schematic of a Bethe Lattice.

There is a significant difference between the two EMT expressions (22) and (23). Numerical simulations will be used to test the validity of the two expressions.

3.2 CRITICAL PATH ANALYSIS

Katz and Thompson [21] developed a model for the single-phase Newtonian permeability k in terms of the rock conductivity σ and a characteristic length l_c

$$k = C{l_c}^2 \frac{\sigma}{\sigma_o} \tag{26}$$

where the constant C is of the order of (1/226) and σ_o is the conductivity of brine in the pore space. The characteristic length l_c can be determined experimentally from the threshold capillary pressure, defined as the point at which the invading mercury, in a mercury injection experiment, first forms a connected path in a rock sample. Expression (26) was developed from the percolation arguments of Ambegaokar et al. [1], which were initially applied to electron transport in amorphous semiconductors. According to this argument, transport in a random system with a broad distribution of conductances (pore sizes) is dominated by those conductances with magnitude greater than some critical value g_c, such that they form an infinite connected cluster in a random system. Katz

and Thompson [21] extended the same percolation idea to the flow of Newtonian fluids in porous media.

Yortsos [53] extrapolated the concept to power-law fluids and derived the following macroscopic law for porous media

$$q^n = \frac{k_1 A k_1^{(n-1)/2} \Delta P}{mL} \tag{27}$$

where the constant A is related to the formation factor σ/σ_o and the exponent n as

$$A = [(\sigma/\sigma_o)^{0.38})\phi^{0.12}]^{n-1} \frac{(7.84)^{1-n} 3^{1+n} (23.57 t_n)^{t_n}}{2^{2n+1}(1+3n)^n (3+t_n)^{2+t_n}}] \tag{28}$$

and for a 3-d network

$$t_n \approx 1.76 + 0.24/n \tag{29}$$

In the above, k_1 is the Newtonian permeability

$$k_1 = \frac{1}{226} l_c^2 \frac{\sigma}{\sigma_o} \tag{30}$$

where l_c is a percolation length obtained from mercury porosimetry. The concept of critical path requires a wide conductance distribution such that substantial flow occurs only over a subset of the pore network close to the percolation cluster. EMT and CPA predictions are the only available theories involving networks of pores where power-law behavior occurs.

3.3 NUMERICAL MODELING OF SINGLE-PHASE POWER-LAW FLOW

The computer simulation of a single phase non-Newtonian fluid was undertaken to understand the flow patterns in network-like porous media for different values of the power-law index n. As mentioned earlier, Sorbie et al. [44] used numerical simulation for the single-phase flow of pseudoplastic fluids in a network-like porous media. Their objective was to understand pore level phenomena for such flow and then proceed to scale up. The objective of our numerical simulation was to test the previous theories, to understand the flow patterns in the single-phase flow of both shear thinning and shear thickening fluids in a network of capillaries and to delineate the departure from the Newtonian behavior (n=1).

In our simulations, the porous media were represented by a 2-D network of capillaries of coordination number 4. The bond length was taken constant, but the capillary radii were randomly distributed. Various wide distributions were considered as required by the CPA approach. Important assumptions in the simulations are that there is no pressure drop in the network due to the nodes and that all the pressure drop across the system is due to the flow in bonds. As before, excess pressure drop associated with entrance and exit flow in each capillary is neglected. The following expression for the single-phase flow of a power-law fluid in a single capillary was used

$$q = \frac{\pi R^{\frac{3n+1}{n}} n \Delta P^{1/n}}{(2LK)^{1/n}(3n+1)} \tag{31}$$

where R and L denote the radius and length of the capillary, respectively. Appropriately rescaled, a dimensionless form of equation (31) reads

$$Q^{\star} = R^{\star \frac{3n+1}{n}} (\Delta P^{\star})^{1/n} \tag{32}$$

where flow rates have been normalized by $\pi \frac{n}{3n+1}(R)^{\frac{3n+1}{n}} \frac{1}{2KL}^{1/n}(P_o - P_1)^{1/n}$, radii by $R^{\frac{3n+1}{n}}$ and pressure differences by $(P_o - P_1)^{1/n}$, with R as a characteristic radius and P_o and P_1 as inlet and outlet pressures of the network.

We next applied mass balances at each node of the network, where the fluid is considered incompressible. Thus, for each node

$$\sum_j Q^{\star}_{ij} = 0 \tag{33}$$

where j runs over all nodes connected to node i. To solve (33), we used successive relaxation methods, with a fairly stringent convergence criteria for shear thinning and shear thickening fluids. The iterative method is detailed in Appendix A. Once the dimensionless pressure field is obtained, we can calculate the normalized flow in each bond using (32). Results for both flow and conductance distribution have been obtained for shear thinning as well as for shear thickening fluids for networks of size 100 × 100. The dimensionless total flow and effective conductance g_m of the network was then obtained to test EMT and CPA theories.

To test the validity of the two EMT equations (22) and (23), we compared the numerical results for g_m obtained for different values of the power-law index n with the values calculated

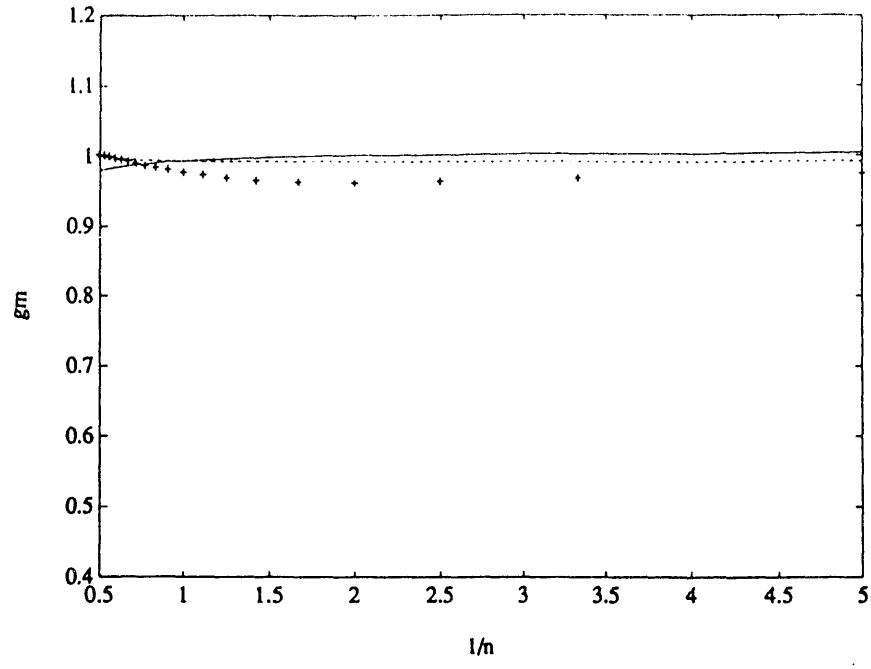

Figure 7: Effective Conductances for Power-law Fluids for a Pore Size Distribution in [0.9-1.1].

from the EMT expressions. We probed their validity for different (uniform) pore size distributions, ranging from narrow to wide. We chose narrow [0.9-1.1], medium [0.4-1.6] and wide [0.01-1.99] distributions, all normalized with a mean pore size of unity. The expression used for calculating g_m for the network size of $N \times M$ reads as

$$g_m = \frac{Q}{M}(N-1)^{1/n} \tag{34}$$

where Q is the flow rate through the network and n is a power-law index.

Figures 7-9 show plots of the effective conductance g_m vs. the power-law index n. Solid lines indicate values of g_m obtained from Cannella and Huh (22), dotted lines show the values calculated from Yortsos (23), while numerical values are plotted as crosses. As shown in Figure 7, the values of g_m calculated from the two analytical expressions are in good agreement with the numerical values obtained from the network for narrow pore size distributions and for a wide range of n, covering both shear thinning and shear thickening fluids. To a certain degree, this result is anticipated from EMT. Expression (23) seems to be fitting the network value more closely, however, and also has the proper trend over the entire range of n. Expression (22) shows the reverse trend for $n>1$. Figure 8 shows a comparisons for intermediate ranges of pore size distributions. Expression (22)

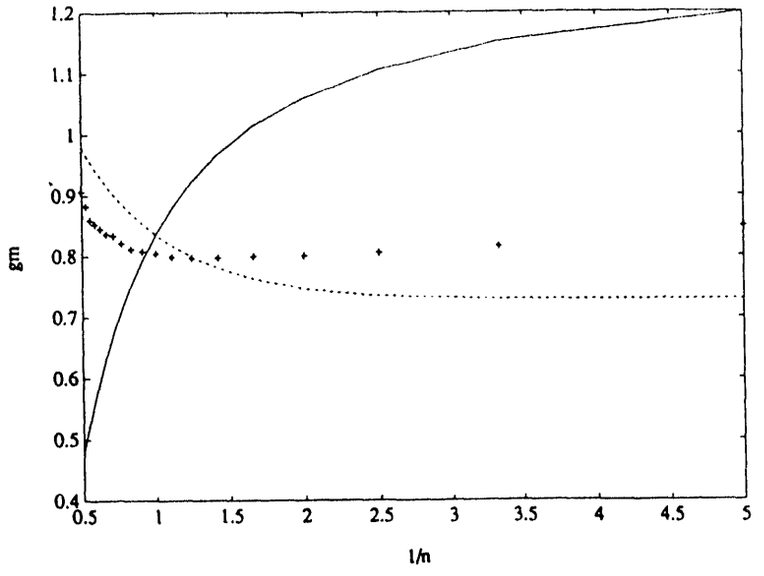

Figure 8: Effective Conductances for Power-law Fluids for a Pore Size Distribution in [0.4-1.6].

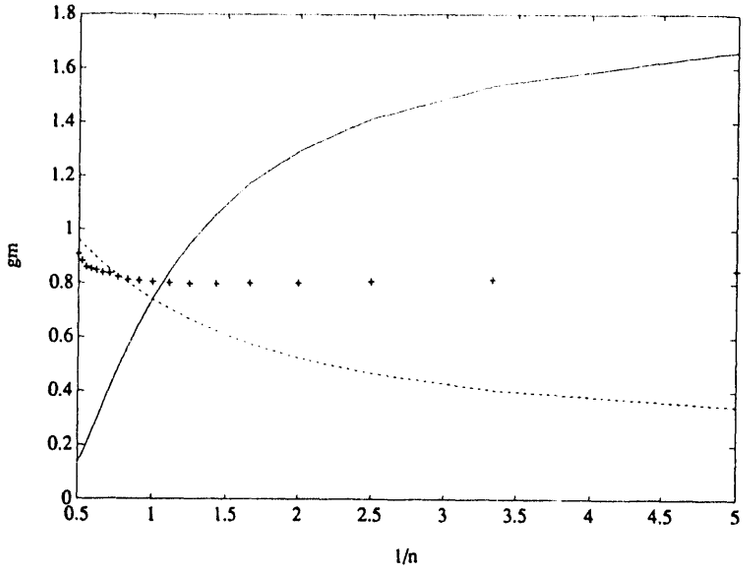

Figure 9: Effective Conductances for Power-law Fluids for a Pore Size Distribution in [0.01-1.99].

developed mainly by qualitative arguments, shows much less agreement with the network results than (23) and also maintains the reverse trend in the shear thickening cases. The values obtained from expression (23) are quite close to the numerical values, which is quite satisfactory considering the degree of approximation involved. One should recall that (23) is a rigorous asymptotic EMT expression for Bethe lattices. Figure 7-8 suggest that it may be also approximately valid for porous media as well, although its applicability should be limited. As the distribution becomes wider, the agreement between analytical and numerical results deteriorates, particularly at low values of n (Figure 7). Even then, expression (23) appears reasonable, provided that the distribution is not very wide. For wide distributions, however, EMT is not expected to be valid. Instead, the critical path analysis is likely to be applicable.

Critical path analysis requires a broad conductance distribution, such that a substantial flow occurs only over a subset of the pore network, which can be taken to be the percolation cluster. To test this approach we considered computer simulations for the flow of power-law fluids in a 3-D 11 x 11 x 11 lattice with power-law index n varying from 0.2 to 2. To test theory and simulation, we rearranged expressions (27) to (30) as follows

$$\log(q^n/D) = \frac{1}{2}[\log k_1 + \log c^2]n + \log B \tag{35}$$

where we defined

$$B = \frac{k_1^{1/2}\Delta P}{cmL}, \tag{36}$$

$$c = (\sigma/\sigma_o)^{0.38}\phi^{0.12}, \tag{37}$$

and

$$D = \frac{(7.84)^{1-n}3^{1+n}(23.57t_n)^{t_n}}{2^{2n+1}(3n+1)^n(3+t_n)^{2+t_n}} \tag{38}$$

In this form, we can directly test the critical path analysis by searching for a linear relation between q^n/D and n in a semilog plot. Figures 10 and 11 show semilog plots of q^n/D against the power-law index n for two different distributions of bond sizes. As can be seen, the theoretical prediction of a straight line in (35) is well satisfied for all values of n that are not too small. We

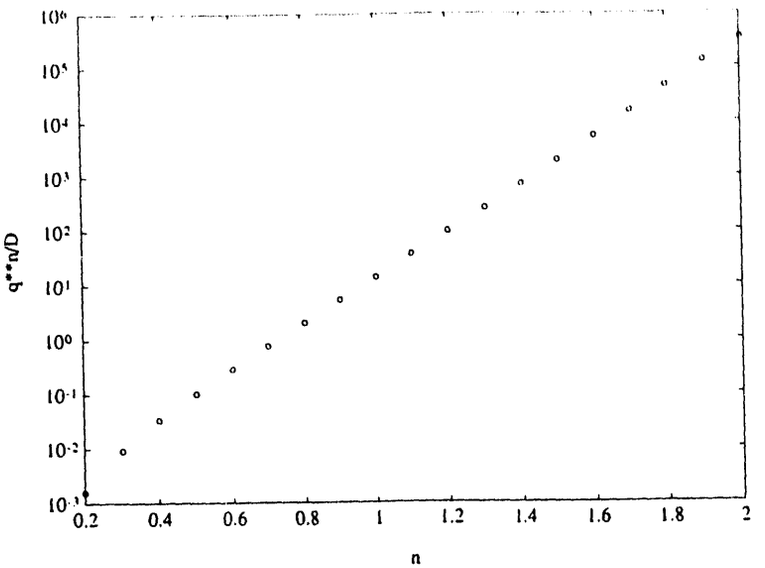

Figure 10: Test of CPA for the Distribution in [0.4-1.6].

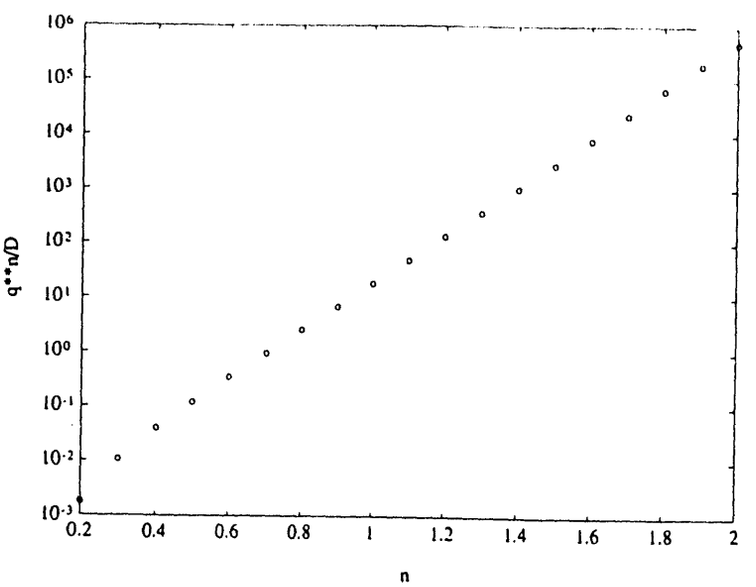

Figure 11: Test of CPA for the Distribution in [0.01-1.99]

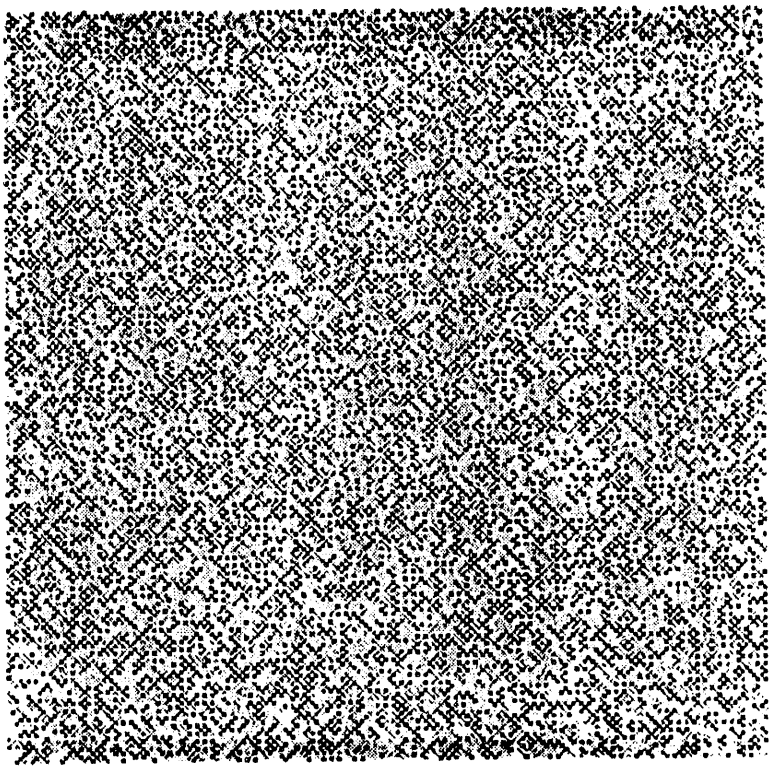

Figure 12: Conductance Distribution for n=1 [0.01-1.99].

do observe, however, a deviation from a straight line behavior for small n. The effect of the pore size distribution is not very significant, both Figures 10 and 11 displaying approximately the same behavior. This can be explained by noting that despite the relatively narrow pore size distribution used in Figure 11, the corresponding conductance distribution, which scales as $r^{3+1/n}$, is still wide, thus satisfying the CPA conditions.

The above simulations in a 3-D lattice confirmed the qualitative accuracy of CPA, except for small values of n. When n is small, a different flow mechanism should be obeyed (see section 4). An illustrative and instructive confirmation of these results is offered by the corresponding flow patterns. In these illustrations, the normalized flow in each bond is denoted with level of grayness proportional to the flow rate through the bond. Thus, black color represents the maximum flow rate, white color corresponds to little or no flow through the bonds of the network. Only flow through the bonds is shown, flow through the nodes connecting two bonds depicted in white. The conductances in the network are also represented in the same manner. Typical results of single phase flow in a network for various values of n are shown in Figures 12-19.

Figures 12-19 show flow and conductance patterns for different values of power-law index with a wide distribution [0.01-1.99]. Figures 12 and 13 show conductances and flow patterns for a

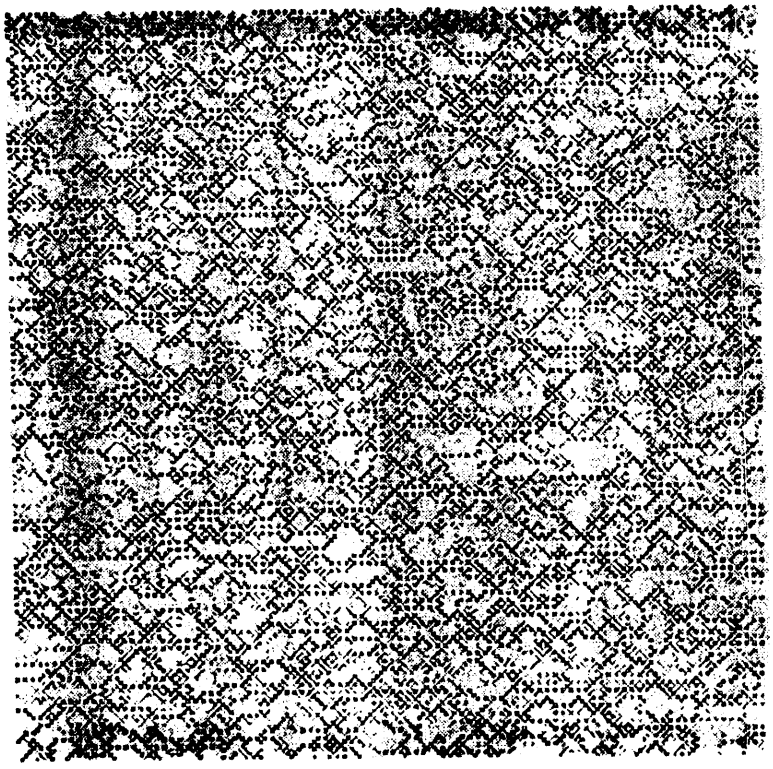

Figure 13: Flow Pattern for n=1 [0.01-1.99].

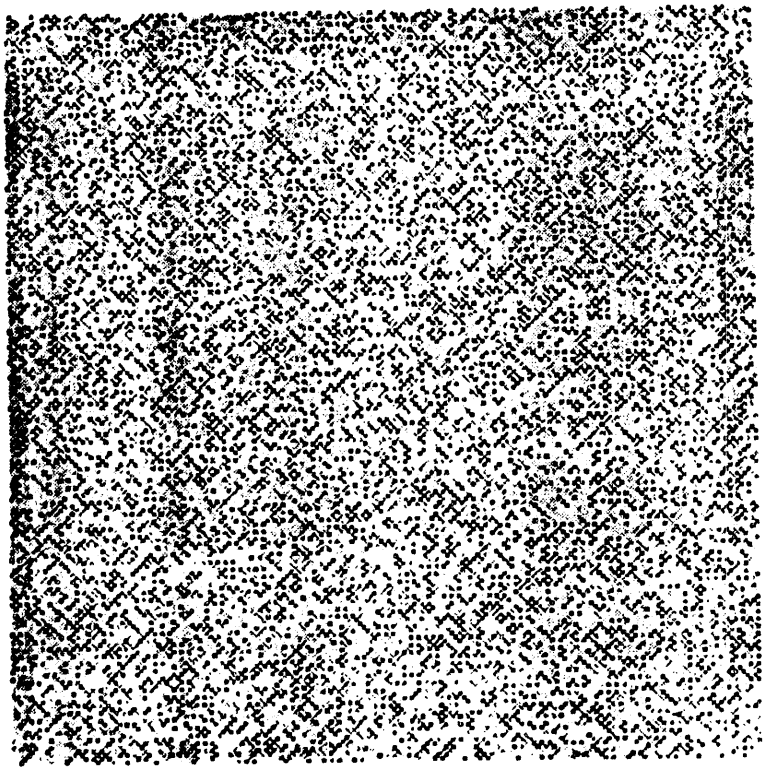

Figure 14: Conductance Distribution for n=0.4 [0.01-1.99].

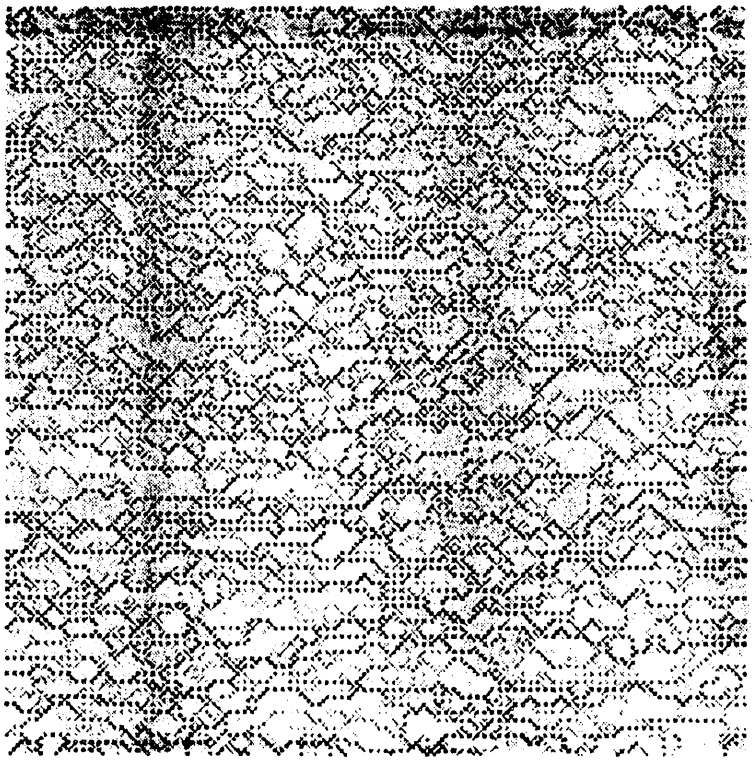

Figure 15: Flow Pattern for n=0.4 [0.01-1.99].

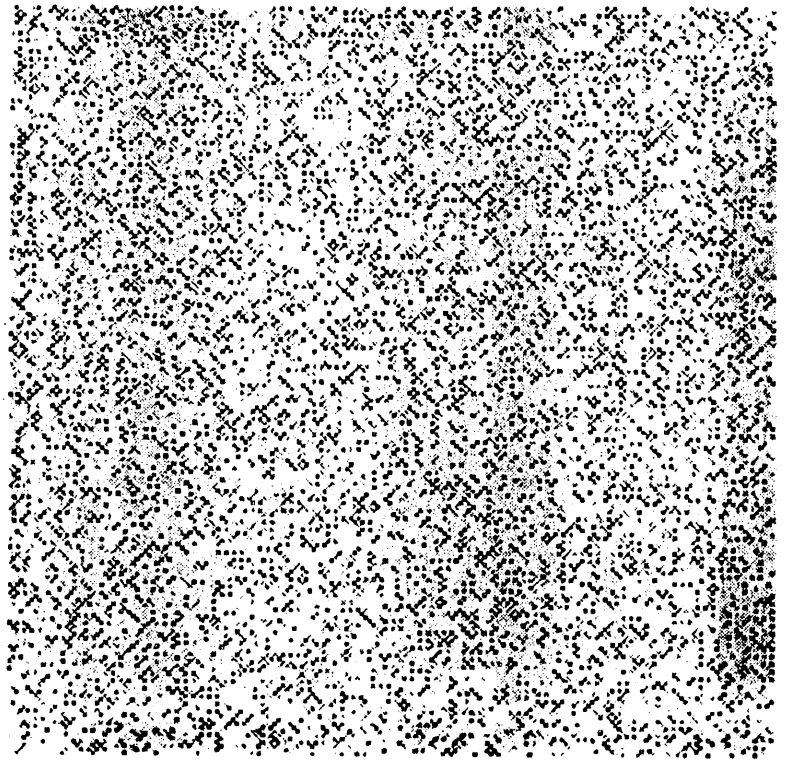

Figure 16: Conductance Distribution for n=0.2 [0.01-1.99].

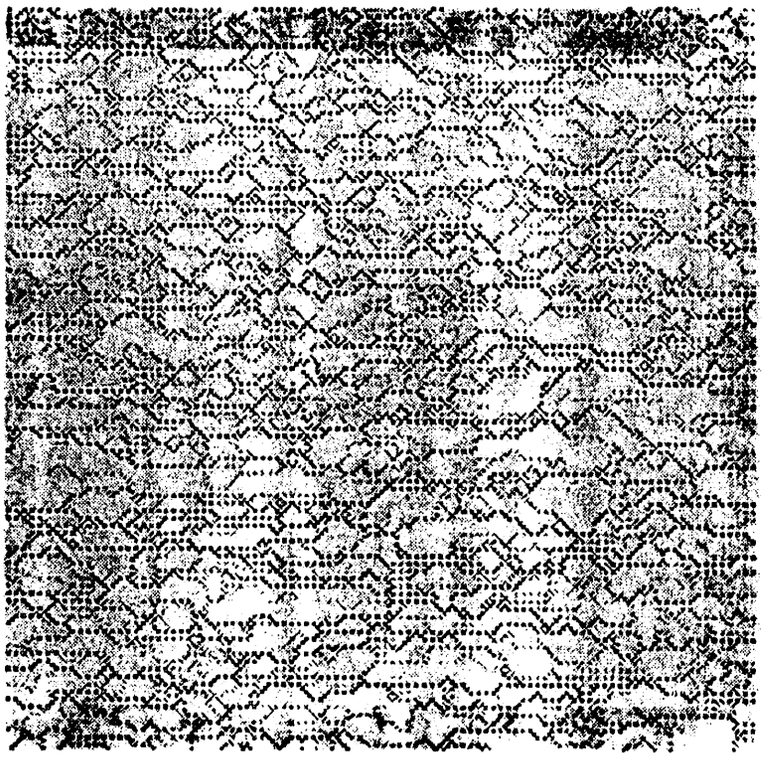

Figure 17: Flow Pattern for n=0.2 [0.01-1.99].

Newtonian fluid ($n = 1$) for comparison purposes. As expected, the conductance distribution is quite wide, the flow being distributed over the entire network. We may identify a connected cluster, resembling a percolating cluster, through which most of the flow is taking place. Indeed, it is apparent that there exist empty pockets (holes), where flow rates are small. The conductance distribution becomes much wider as we decrease the value of n, because of the relation $g \approx r^{3+1/n}$. A typical example for $n = 0.4$ is shown in Figures 14 and 15. The flow occurs through a limited network of connecting bonds with most of the flow occuring through few connected paths. We can also identify large empty pockets, where no flow takes place, in accordance with the theory. Similar results were also obtained for n=0.8 and 0.6 (not shown), indicating that shear thinning fluids in this range flow through the network as expected from CPA. At smaller values of n, the conductance distribution is very wide and flow occurs only through a small subset of the percolating cluster corresponding to the highest conducting bonds. The subset becomes smaller as n decreases [4, 5] (Figures 16 and 17). In this case, the entire flow occurs through a very small number of connected bonds. The remaining network contributes very little to flow and it is almost impermeable. Clearly, the application of effective medium theories would be fruitless in such situations. The existence of a critical path requires that the conductance distributions are wide. Since the conductance is

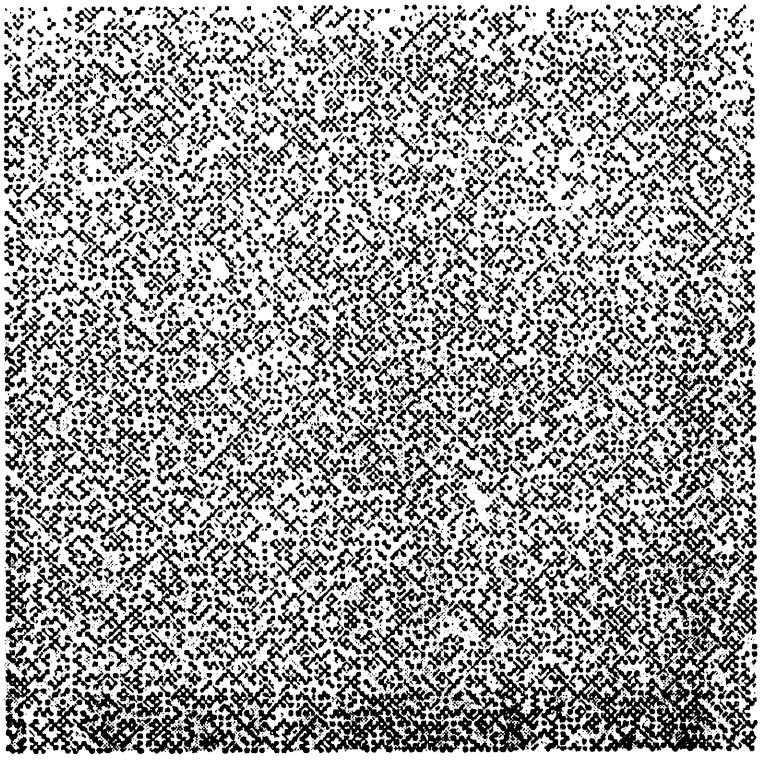

Figure 18: Conductance Distribution for n=2 [0.01-1.99].

related to the bond size through $g \approx r^{3+1/n}$, such a hypothesis is satisfied better as n decreases. Nonetheless, shear thickening fluids also qualify for an application of CPA. Figures 18 and 19 show the conductance and flow patterns for a shear thickening fluids (with $n = 2$), where, as expected, the flow distribution resembles the Newtonian case ($n = 1$).

The above confirm quantitatively the validity of the critical path analysis, particularly for shear thinning fluids. When n becomes very low the application of the theory is questionable, as already anticipated in [53]. In fact, this case is similar to the flow of Bingham plastic in porous media, which is subsequently discussed.

4 FLOW OF BINGHAM PLASTICS IN POROUS MEDIA

Bingham plastics exhibit a finite yield stress at zero shear rate and have been used to model the flow of some heavy oils. Laboratory investigations and field tests have indicated that flow of heavy oil takes place only after the applied pressure gradient exceeds a certain minimum value [33, 52]. Also, flow of groundwater in certain clayey soils, flow of foam in porous media, flow of certain drilling and hydraulic-fracturing fluids, all exhibit rheological behavior that in certain instances

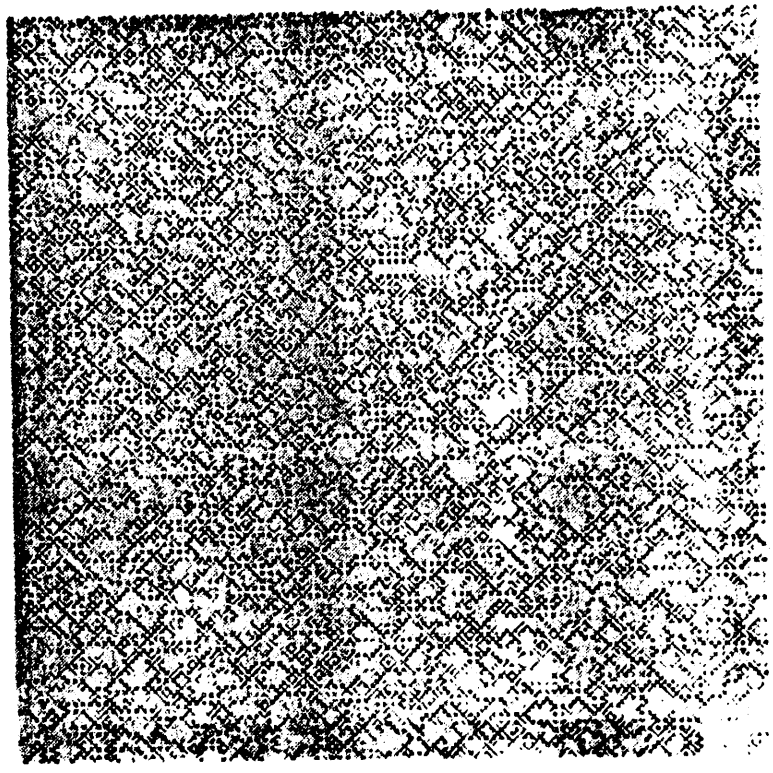

Figure 19: Flow Pattern for n=2 [0.01-1.99].

can be described as a Bingham plastic.

The simulation procedure for the single-phase flow of Bingham plastic in a network-like porous media is the same as outlined in Section 3, except that the governing equations for the flow are different and more difficult to solve. The expression for the flow of Bingham plastic in a capillary is given by [3]

$$q = \frac{\pi R^4}{8\mu_o L}(1 - \frac{4}{3}(\frac{\tau_o}{\tau_R}) + \frac{1}{3}(\frac{\tau_o}{\tau_R})^4)\Delta P \text{ when } \tau_R > \tau_o, \tag{39}$$

and by

$$q = 0 \text{ when } \tau_R < \tau_o \tag{40}$$

where R and L denote radius and length of the capillary respectively, q is the volume flow rate in a pore, across which there is an applied pressure drop ΔP and τ_R is the wall shear stress.

Appropriately rescaled, the dimensionless form of the equations are

$$q^* = R^{*4}(1 - \frac{4}{3}(\frac{\tau_o}{\tau_R}) + \frac{1}{3}(\frac{\tau_o}{\tau_R})^4)\Delta P^* = g^*\Delta P^* \text{ when } \tau_R > \tau_o, \tag{41}$$

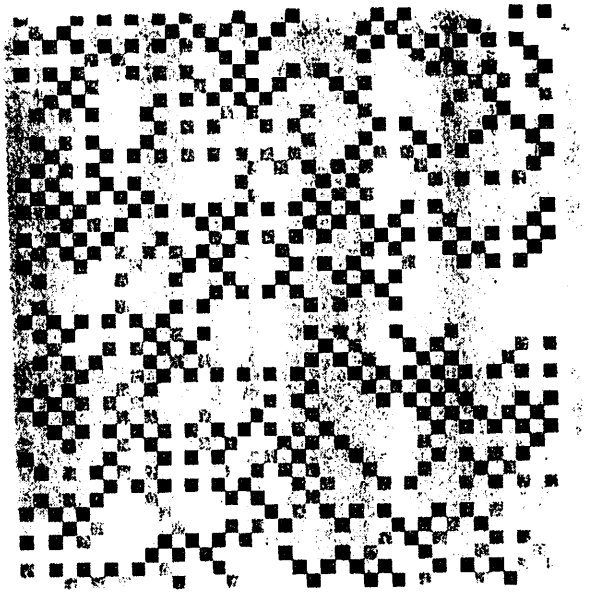

Figure 20: Flow Pattern for $\tau_o = 0$ [0.01-1.99].

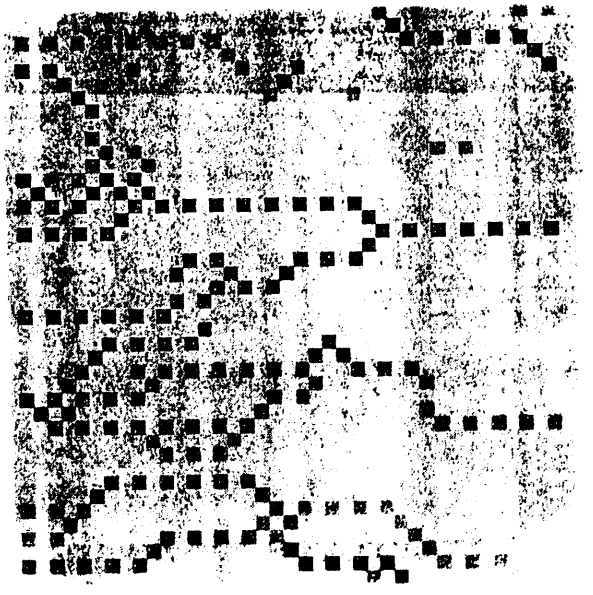

Figure 21: Flow Pattern for $\tau_o = 0.01$ [0.01-1.99].

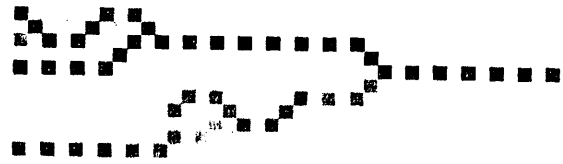

Figure 22: Flow Pattern for $\tau_o = 0.05$ [0.01-1.99].

and

$$q^* = 0 \text{ when } \tau_R < \tau_o \tag{42}$$

where g^* is a dimensionless conductance for a single capillary and

$$\tau_R = \frac{\Delta P R}{2L} \tag{43}$$

The pressure field in the network was calculated by applying a successive relaxation iteration method. Results for the flow and conductance distributions have been obtained for Bingham plastic fluids in networks of size 21 x 21. Two uniform size distributions, a narrow and a wide were used.

Figure 20 shows the flow pattern of a Newtonian fluid ($\tau_o = 0.0$) in a uniform distribution of bond sizes in the interval [0.01-1.99]. We observe that the flow is distributed over the entire network, and we may identify a connected cluster, resembling a percolating cluster, through which most of the flow is taking place. Figure 21 represents the corresponding flow pattern for Bingham plastic fluid with the value of yield stress equal to 0.01. We observe additional empty pockets in the network as more bonds in the network become non-conducting due to the higher value of yield

Figure 23: Flow Pattern for $\tau_o = 0.065$ [0.01-1.99].

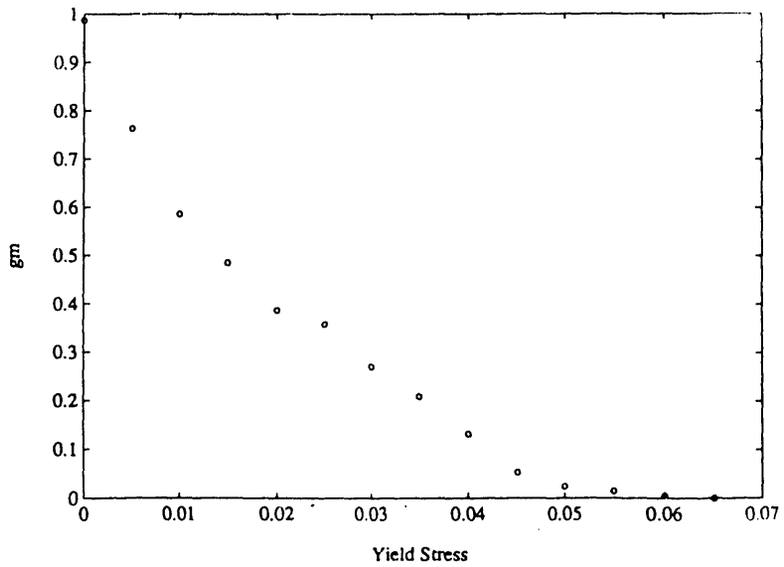

Figure 24: Critical Yield Stress [0.01-1.99].

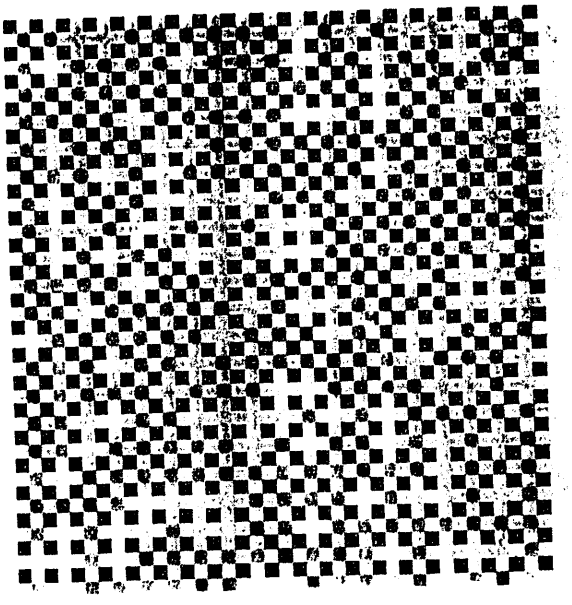

Figure 25: Flow Pattern for $\tau_o = 0$ [0.9-1.1].

stress. As it is not possible to accommodate all the simulation results in this report, two typical examples are shown in Figures 22 and 23, where the values of yield stress are 0.05 and 0.065, respectively. In Figure 22, flow occurs only through a limited network of connecting bonds. We identify large empty pockets in the network, where no flow occurs. We observe more pronounced effects when $\tau_o = 0.065$, where the entire flow occurs through a very small number of connected bonds. The remaining network has a limited participation to flow and behaves much like an empty pocket. These results are similar to those obtained for shear thinning fluids when the value of power-law index is small [41]. Figure 24 shows a plot of the effective conductance versus yield stress. We can identify a macroscopic critical yield stress beyond which the flow is zero.

The other case involves a narrow size distribution [0.9, 1.1]. Figure 25 shows flow patterns for the Newtonian fluid ($\tau_o = 0$). The flow is quite uniform throughout the entire network and we do not observe many empty pockets. Flow is taking place mainly along the pores in the flow direction and very limited flow is observed in the transverse direction. As we increase the value of the yield stress (Figure 26) all flow occurs basically through straight paths, each connecting the same number of pores. Figure 27 indicates flow patterns for larger values of the yield stress τ_o=0.045, where flow takes place through only a few horizontal paths and the rest of the network is non-conducting.

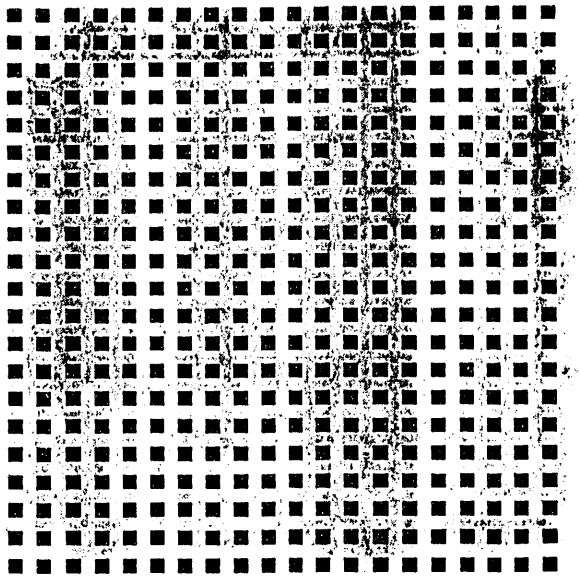

Figure 26: Flow Pattern for $\tau_o = 0.01$ [0.9-1.1].

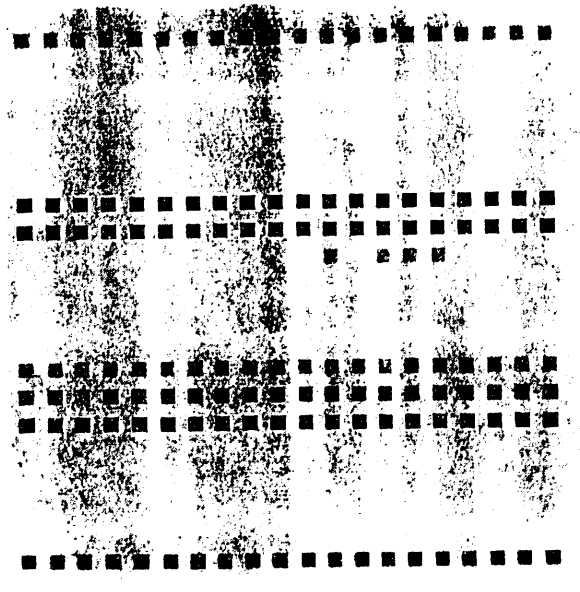

Figure 27: Flow Pattern for $\tau_o = 0.045$ [0.9-1.1].

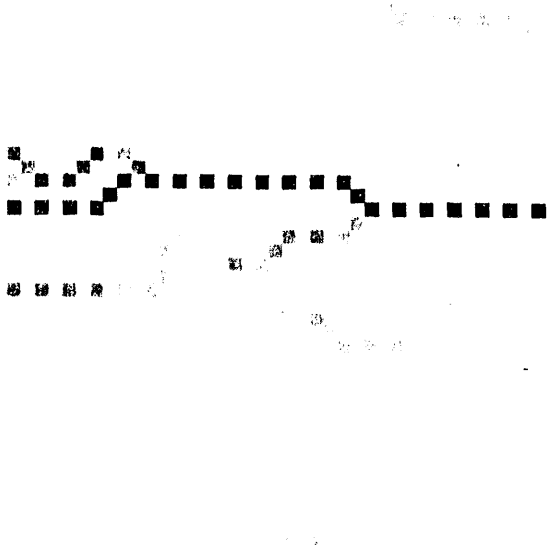

Figure 28: Flow Pattern for n=0.07 [0.01-1.99].

We suggested earlier that the flow behavior of shear thinning fluids with small n would be similar to the flow of a Bingham plastic. To test this argument, typical flow patterns for the single-phase flow of shear thinning fluid, with n=0.07, for the same network size and distribution used for Bingham plastic, are shown in Figure 28. We observe a striking similarity in the flow patterns with the patterns of Figure 22 corresponding to a Bingham plastic with τ_o=0.05. This analogy, however, needs to be tested further.

5 IMMISCIBLE DISPLACEMENT INVOLVING POWER-LAW FLUIDS

The previous sections dealt with single phase flow. In this section, we consider two phase flow and displacement. First, we will simulate the displacement of a Newtonian fluid by a power-law fluid in a drainage process. The long-term goal of this study is to examine the displacement patterns obtained for various types of non-Newtonian fluids and proceed with scale-up. We have mainly concentrated on shear thinning fluids. In the case of Newtonian fluids, it is common practice to relate displacement patterns to the viscosity ratio of the two fluids (stable vs. unstable). However,

the viscosity of power-law fluids changes depending on the applied shear rate and it is varying from bond to bond in the network. Therefore, the previous results do not apply and must be modified. In modeling such immiscible displacement through the network, we have used the following standard assumptions [26]: (i) Volume calculations apply to pore bodies only, the pressure drop occurring in pore throats. (ii) Throats are filled by either invading or displaced fluids, while bodies may contain both fluids. (iii) The capillary pressure in a throat is inversely proportional to the tube radius, while the capillary pressure drop in a node is negligible. Two cases were considered, one involving constant pressure and another involving constant flow rate.

In the simulations we have considered the drainage of a wetting Newtonian fluid by injecting a non-wetting power-law fluid. When the bonds in the network are occupied by the Newtonian fluid, Poisseuille's law for the flow rate Q_{ij} across each bond connecting adjacent nodes i and j applies

$$Q_{ij} = \frac{\pi R_{ij}^4 (P_i - P_j)}{8\mu L_{ij}} = g_{ij}(P_i - P_j) \tag{44}$$

where P_i is the nodal pressure, R_{ij} and L_{ij} are the radius and length of the bond, respectively, and μ is the viscosity of the Newtonian fluid.

The pressure field in the network is calculated by applying the mass balance equation (33) at each node as described in the simulation of single-phase flow. The non-wetting fluid (non-Newtonian in this case) cannot enter a bond unless the pressure difference across that bond exceeds a threshold pressure P_c, given by Laplace's law

$$P_c = \frac{2\gamma}{R_{ij}} \tag{45}$$

where γ is the interfacial tension. Hence, a particular bond is invaded if there is no trapping and the capillary pressure condition is satisfied. Once the bond is invaded, the governing flow equation in the bond changes to

$$Q_{ij} = \frac{\pi R_{ij}^{(3n+1)/n} n (P_i - P_j)^{1/n}}{(2L)_{ij}^{1/n}(3n+1)K} = g_{ij}\Delta P_{ij}^{1/n} \tag{46}$$

hence, the value of g_{ij} depends on both the power-law index n and the consistency index K. In the subsequent steps for pressure calculation, the same iterative method is applied, except that we use a combination of linear and non-linear flow equations depending on the type of the fluid present in

each bond of the network. The node saturation is updated at each time step using (46). In time Δt the node saturation $S_i(t)$ increases as follows

$$S_i(t + \Delta t) = S_i + \Delta t V_i \sum_j Q_{ij} \tag{47}$$

where V_i is the volume of node i. The time interval Δt is calculated such that only one node is filled at each time step. For the next time step, the calculations are repeated and the flow of the two immiscible fluids is solved. Two dimensionless groups emerge depending on the boundary conditions and they are defined as follows (APPENDIX B)

$$N_{caP} = \frac{R^2 \Delta P}{N L_{ij} \gamma} \tag{48}$$

where N_{caP} is the capillary number for constant pressure displacement

and

$$Ca = \frac{Q_D N N_{caP}}{8M} \tag{49}$$

where Ca is the capillary number for constant rate displacement. Here, Q_D is the dimensionless flow rate calculated for an $N \times M$ network.

5.1 CONSTANT PRESSURE DROP DISPLACEMENT

Simulation results were used to understand the effect of power-law index n on displacement patterns. For convenience, we have chosen the value of consistency index K to be the same as the viscosity of the Newtonian fluid for all the values of n used. As the simulation procedure involves highly nonlinear iterative calculations, networks of small size (25 x 25) were selected. The results were verified with larger networks of size 100 x 100 in few cases, however, to ensure their validity. The simulation patterns reported below are for two values of N_{caP}. In all Figures, black color refers to the Newtonian fluid and white color represent the invading non-Newtonian fluid.

Figure 29 shows displacement patterns for n=1 (Newtonian fluid) which serves as a basis of comparison with different values of n (with N_{caP}=0.02). The mobility ratio for this case is unity and we observe more or less stable displacement in this range of capillary number (10^{-3}) in agreement with Lenormand et al. [26]. Typical results of two-phase flow in the network for both shear

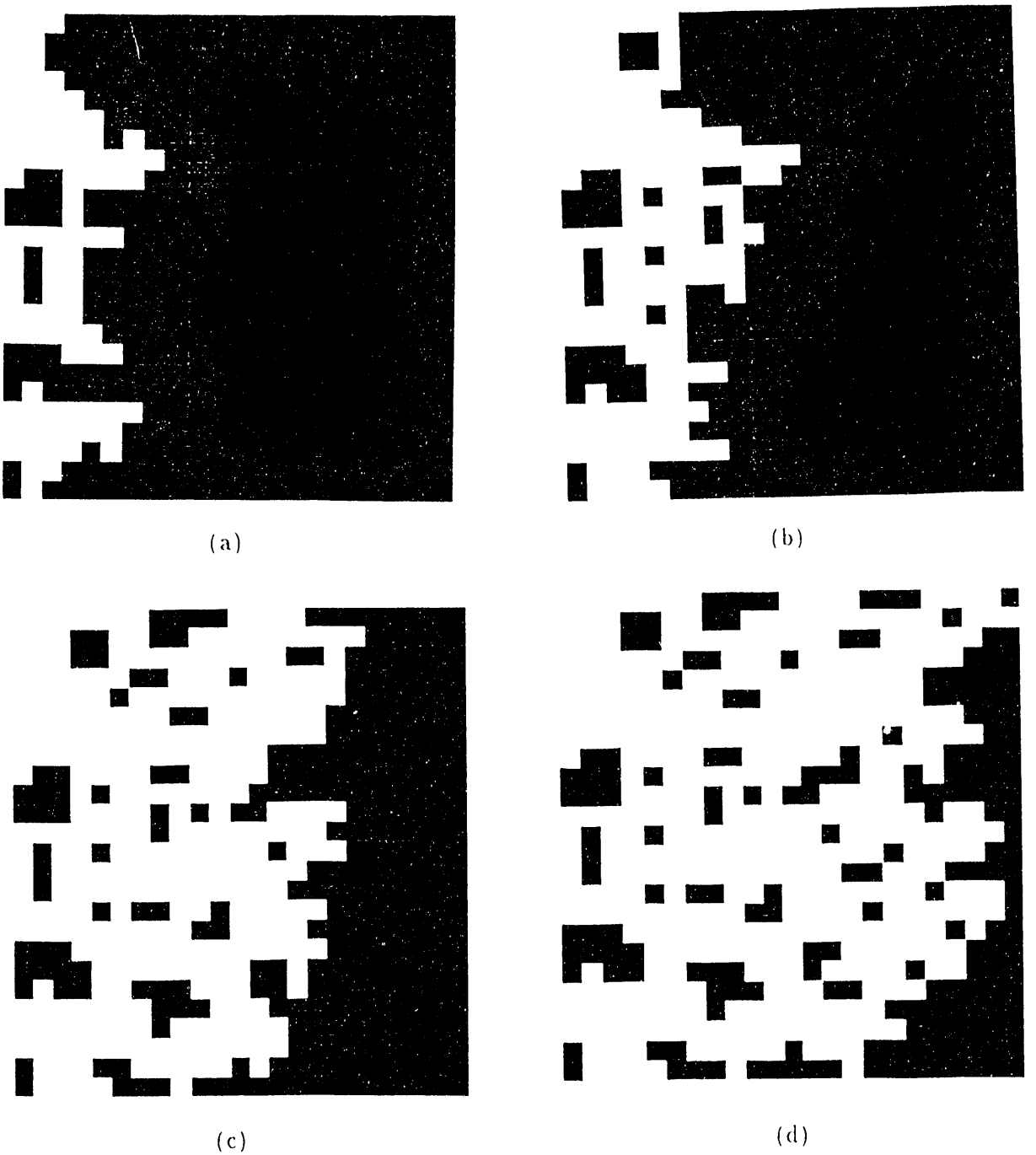

Figure 29: Immiscible Displacement for n=1 (N_{caP} = 0.02) at Four Different Time Steps (a) 90 (b) 150 (c) 300 (d) 390.

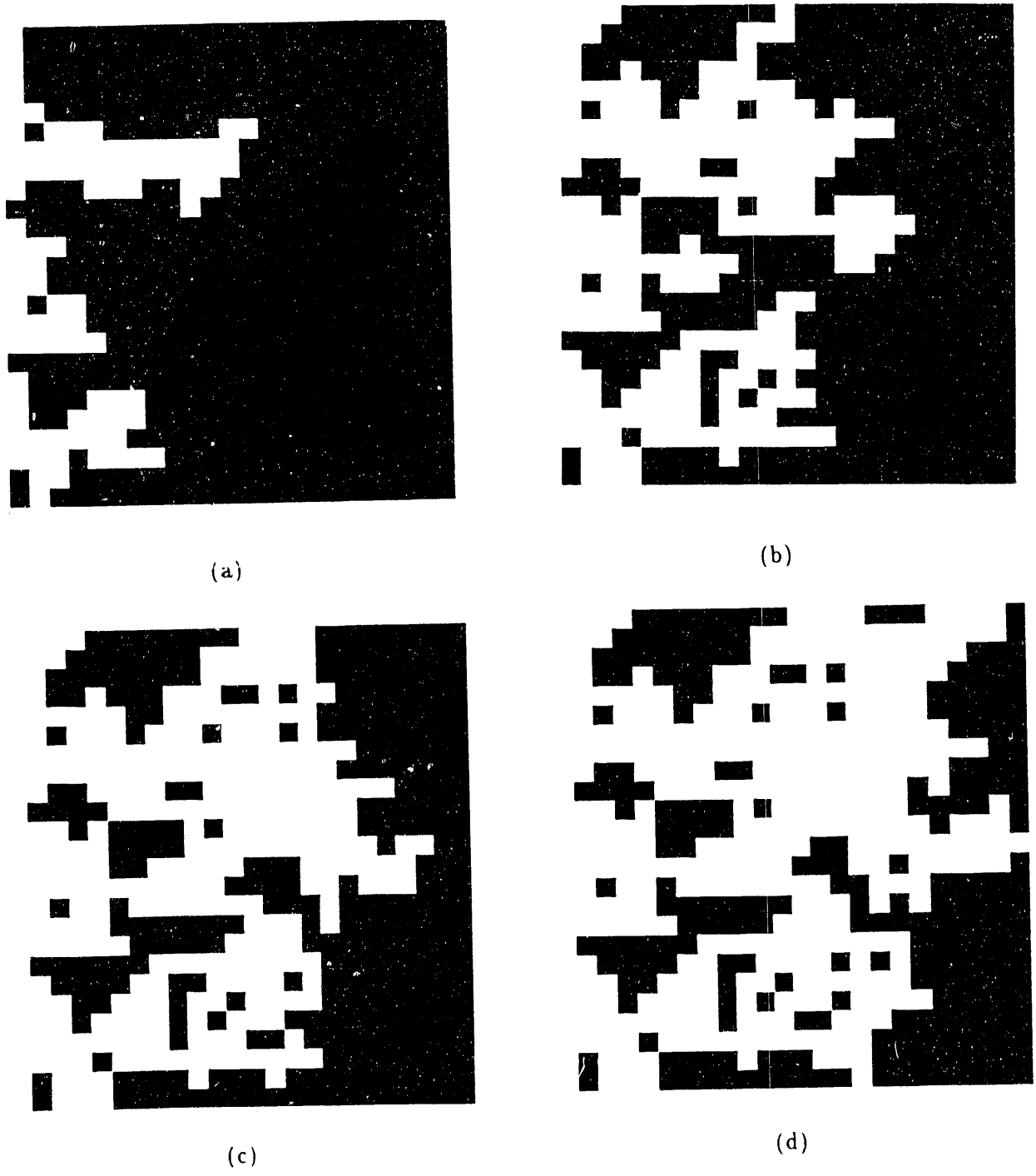

Figure 30: Immiscible Displacement for n=0.8 (N_{caP} = 0.02) at Four Different Time Steps (a) 90 (b) 210 (c) 270 (d) 330.

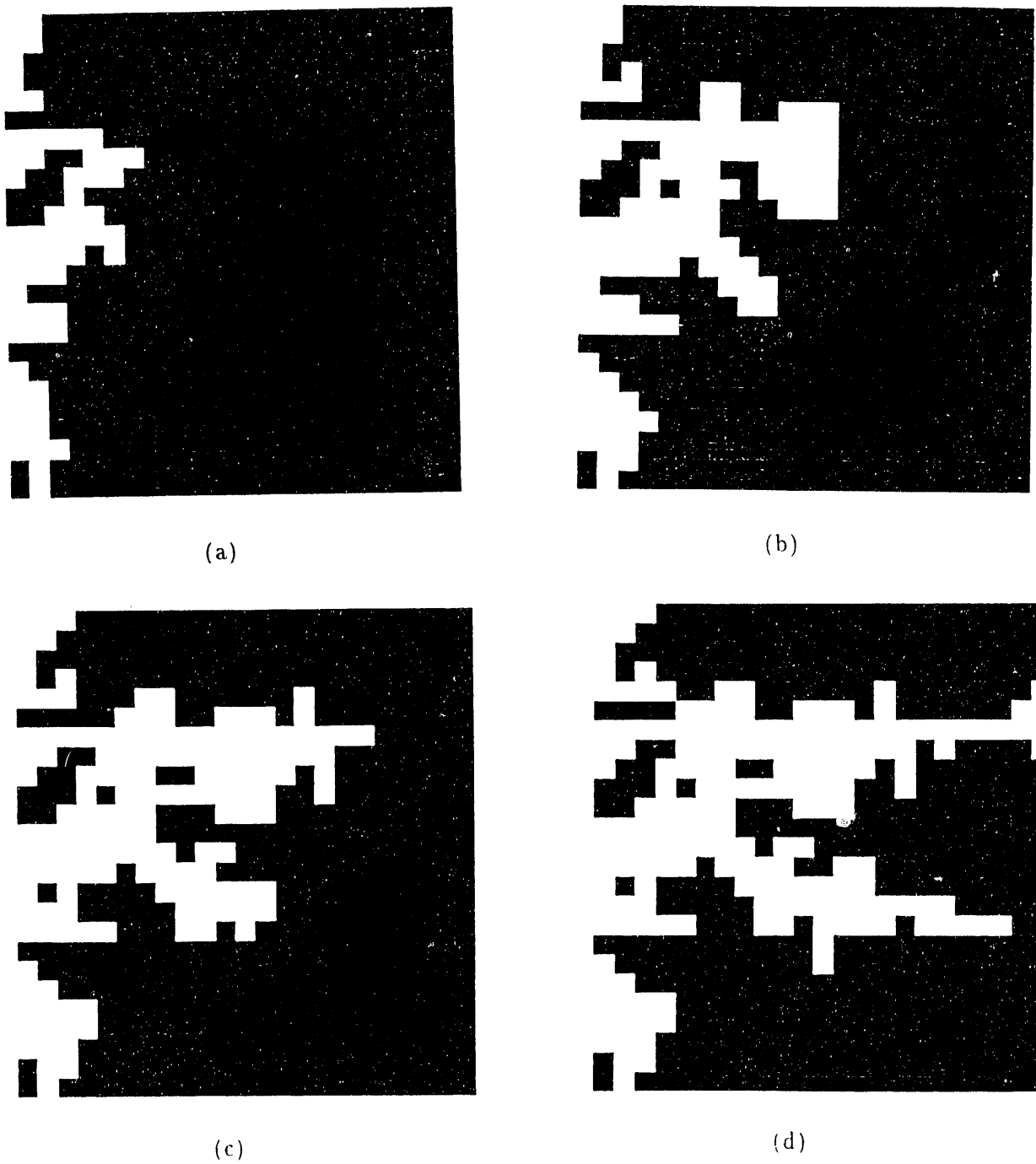

Figure 31: Immisccible Displacement for n=0.4 (N_{caP} = 0.02) at Four Different Time Steps (a) 60 (b) 120 (c) 150 (d) 180.

thinning (n = 0.8, 0.4 and 0.2) and shear thickening (n = 1.5) are shown in Figures 30-33 for the same capillary number. In all Figures, four displacement patterns (a)-(d) are shown at different time steps.

Figure 30 shows displacement patterns for shear thinning fluids with n = 0.8. We observe patterns quite similar to the Newtonian case although we see little tendency for fingering and trapping during displacement. The pattern is very close to that of unstable displacement. Further lowering of the power-law index shows instability (Figure 31, n = 0.4), the interface advancing with large fingering and bypassing. Viscous fingers, developed right after the onset of flow, penetrate rapidly through the Newtonian fluid. For n=0.2, the flow of the invading fluid increases rapidly through the network and we see faster movement of the fingers. In general, we observe excessive tendency for fingering, trapping and bypassing in the shear thinning case, particularly at low values of n. These results are consistent with the previous flow patterns of single-phase flow (Figures 11-19). Indeed, one would anticipate that the shear thinning fluid would select a narrow flow path, and thus show a pronounced tendency for fingering. The opposite picture develops for the shear thickening case (Figure 33, n=1.5). It is observed that the interface is quite compact with a very small amount of trapping at the indicated capillary number. In these constant pressure drop simulations, the capillary number Ca increases as the shear thinning fluids advances through the network (Figure 34). The increase is very steep for smaller values of n as can be predicted from the macroscopic law for power-law fluids. For the shear thickening case, on the other hand, Ca decreases with time.

In the above, we found excessive fingering and tendency for unstable displacement as n decreases. As is the case with Newtonian fluids, this can be explained in terms of the mobility ratio. We decrease the value of n, the shear thinning tendency of the fluids is more visible, the mobility ratio, being the ratio of the viscosity of the Newtonian fluid to the average effective viscosity of shear thinning fluid, increasing dramatically. Typical simulation results for n=0.2 but with different viscosity for the Newtonian fluid (0.001 poise) are shown in Figure 35 for a 50 $\times$ 50 network. We observe that the tendency for fingering and bypassing is still unabated. In all these results, the capillary number N_{caP} is equal to 0.1 for the displacement to be purely viscous. For such small values of n the pattern is one of unstable displacement dominated by viscous fingering, irrespective of the displaced phase viscosity in the observed range. After a certain time, which varies with N_{caP},

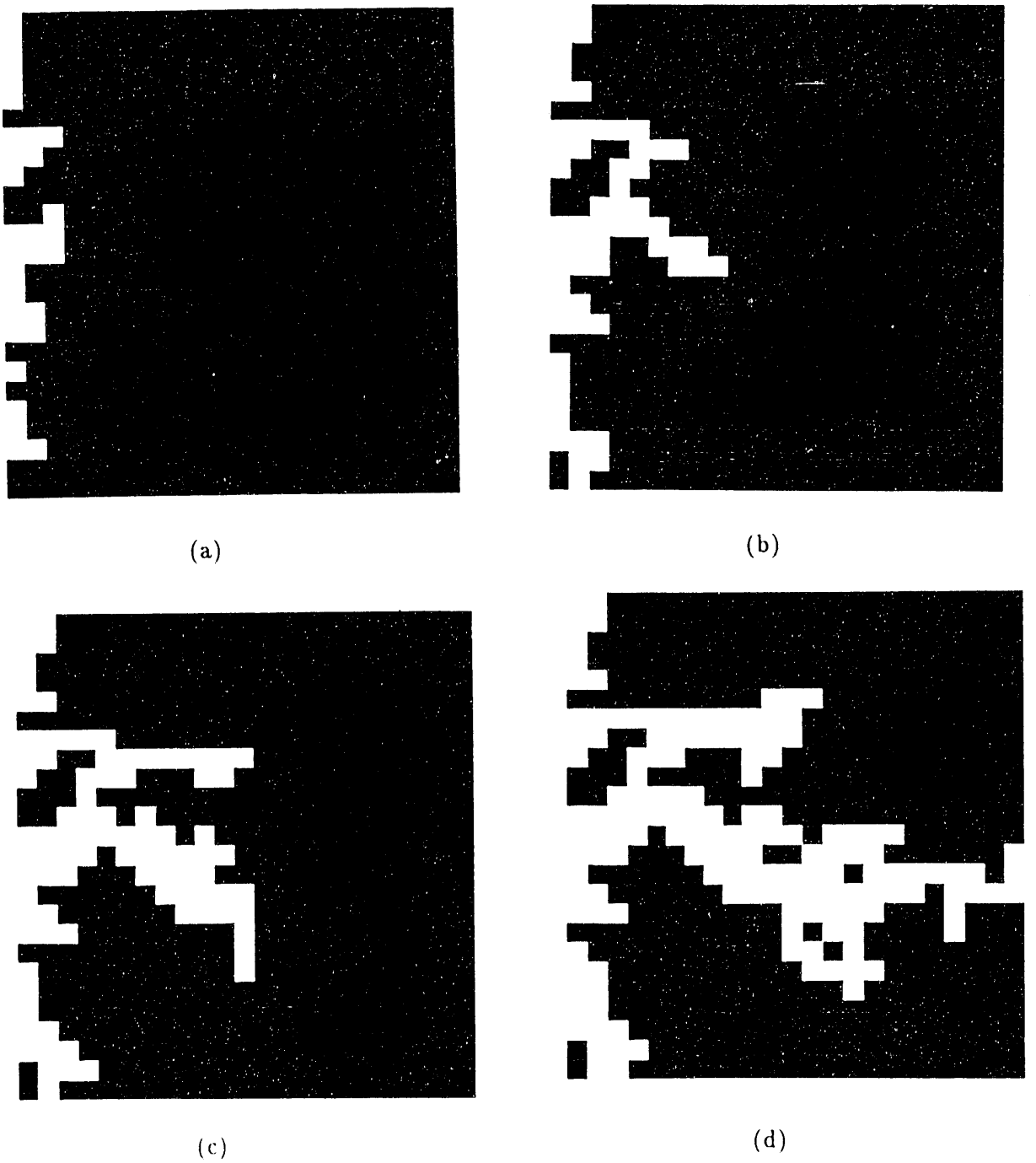

Figure 32: Immisccible Displacement for n=0.2 (N_{caP} = 0.02) at Four Different Time Steps (a) 30 (b) 60 (c) 90 (d) 120.

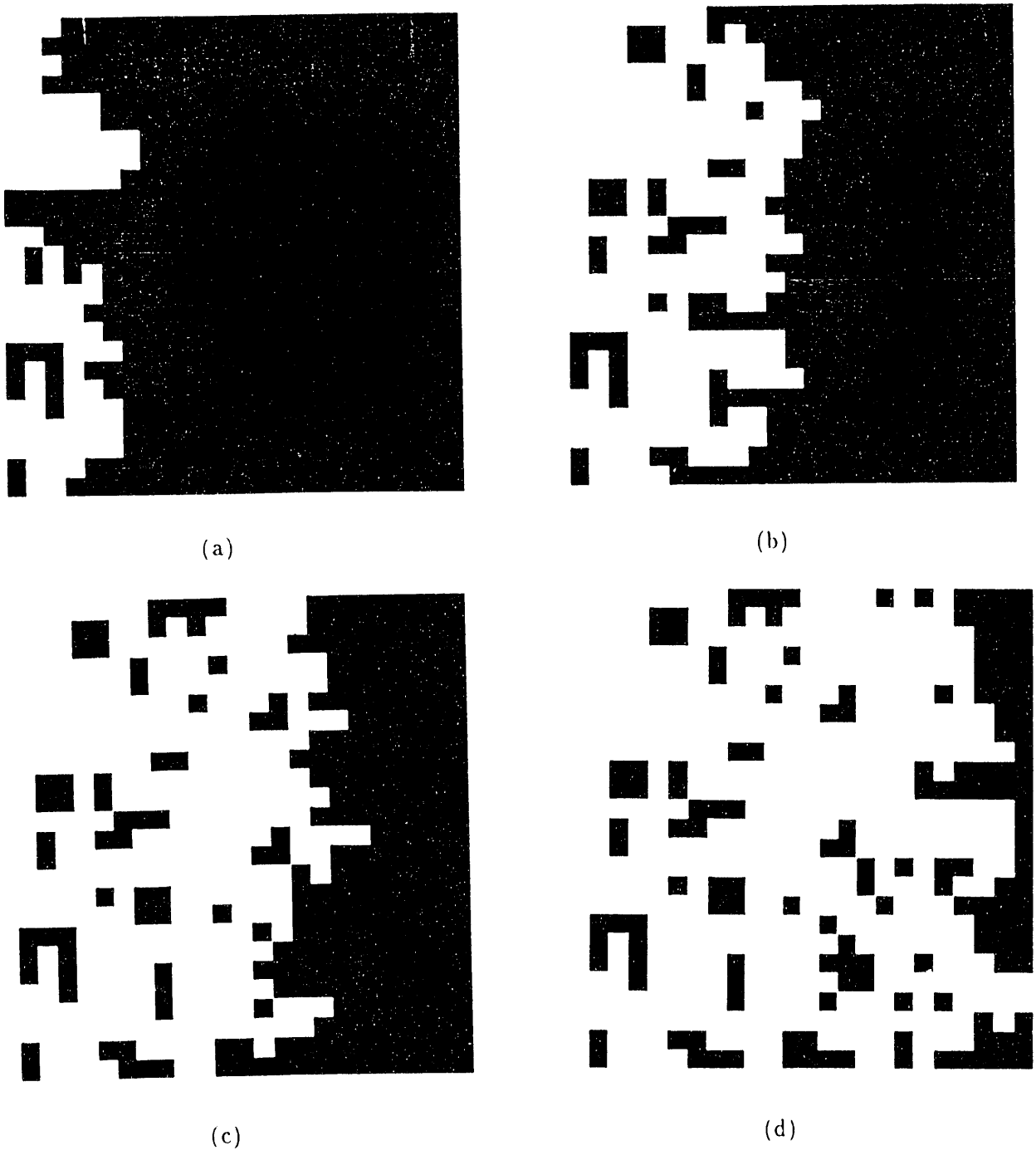

Figure 33: Immisccible Displacement for n=1.5 (N_{caP} = 0.02) at Four Different Time Steps (a) 90 (b) 150 (c) 300 (d) 420.

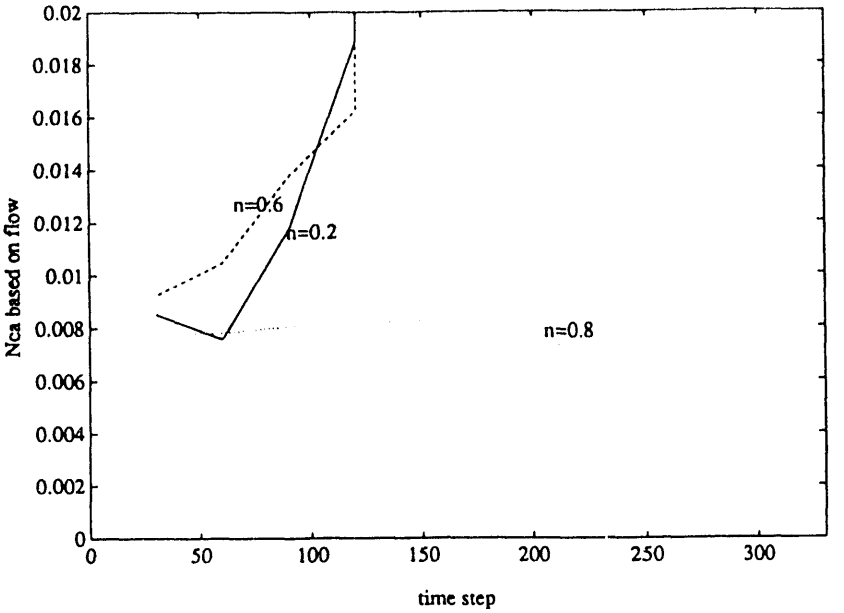

Figure 34: Change in Ca with Time Step for $n < 1$.

the finger accelerates and a very high value of flow rate through the network is obtained.

5.2 CONSTANT FLOW RATE DISPLACEMENT

In the constant flow rate problem, the invading fluid is injected at a constant rate through the inlet face, while the pressure at the outlet face is constant. This type of displacement is of great practical interest. Values of the power-law parameters K and n based on [7] were used in the numerical simulation. Before we proceed with the numerical simulations, we shall describe some macroscopic results.

Pascal [31, 29, 30, 28] reported a theoretical work on the stability of a moving macroscopic interface in porous media in the case of immiscible displacement at a constant rate for power-law fluids. In the absence of gravitational and capillary effects, the stability condition reads

$$\frac{\mu_2}{k_2}V - \frac{\mu_{eff}}{k_1}V^n < 0 \tag{50}$$

and if we assume $k_1 = k_2$,

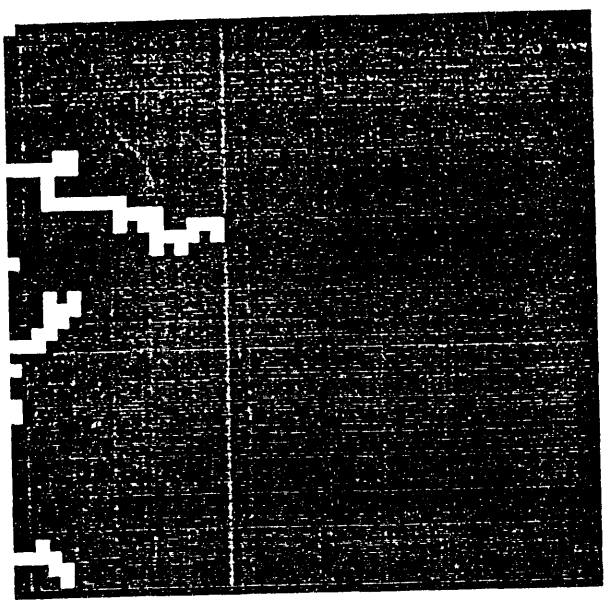

(a)

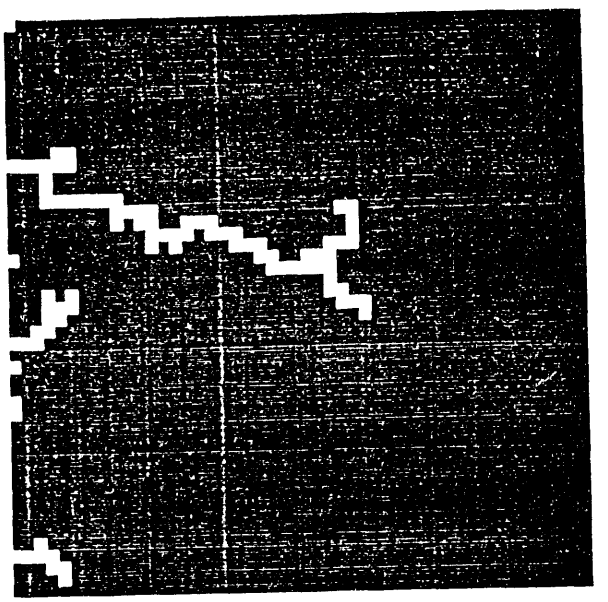

(b)

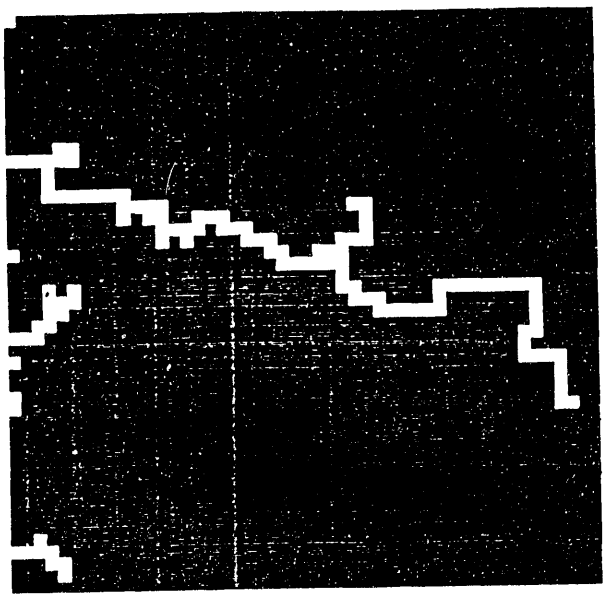

(c)

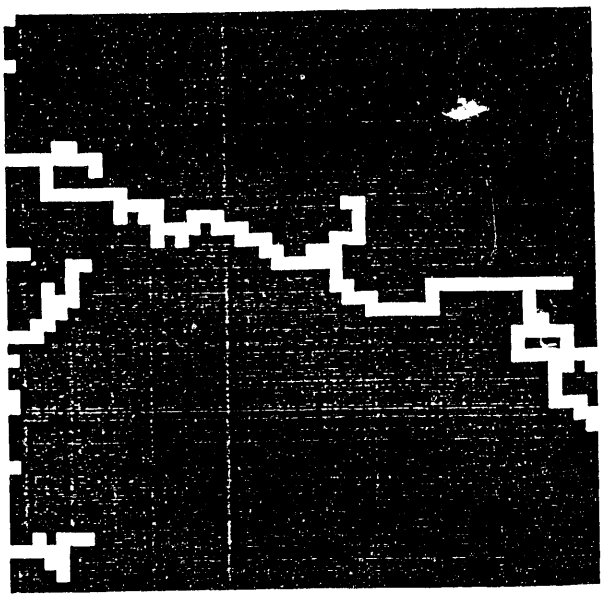

(d)

Figure 35: Immiscible Displacement $\mu = 0.001$ ($N_{caP} = 0.1$) at Four Different Time Steps (a) 60 (b) 90 (c) 120 (d) 150.

$$\frac{\mu_2}{\mu_{eff}} V^{1-n} < 1 \tag{51}$$

Thus, stability requires V to be low for shear thinning fluids ($n < 1$) and high for shear thickening fluids ($n > 1$). This prediction is to be tested in the pore network displacement process.

To characterize the non-linear immiscible displacement, the following dimensionless number is introduced

$$N_P = \frac{q}{R(\frac{K}{\mu})^{\frac{1}{1-n}}} \tag{52}$$

where q is the flow velocity, R is a characteristic radius of the network and K and n are the usual power-law parameters. The simulation procedure is as described in the case of constant pressure. The major difference is that to maitain a constant injection rate. The following mass balance at the inlet face must be solved

$$\sum_{k=1}^{M} g_k (P_{in} - P_k)^{1/n} = Q \tag{53}$$

where P_{in} is the pressure at the inlet face, P_k is the pressure at the nodes adjacent to the inlet nodes and Q is the prescribed constant flow rate. P_{in} is calculated iteratively until convergence. We typically use a network of size 25 x 25.

Numerical simulations were carried out for four different types of shear thinning fluids for the parameters of Table 1. The displacement patterns are for two types of shear thinning fluids and for a wide range of capillary numbers. The power-law parameters n and K are 0.35 and 6.20 $Psec^{n-1}$ for the first invading fluid, which is highly shear thinning in nature. A similar set of results is also reported for the other fluid with $n = 0.6$ and $K = 0.43$ $Psec^{n-1}$, which can be considered as moderately shear thinning. The simulations were made to understand the effects of capillary number and power-law parameters on the displacement patterns.

Figures 36 to 37 show displacement patterns for the first case. Figure 36 shows the displacement at four different time steps for a high value of the capillary number (Ca=3.33 x 10^{-1}). At such high velocity, the displacement is similar to the viscous fingering domain of a Newtonian fluid. As the injection rate decreases to Ca=3.33 x 10^{-4}, (Figure 37), we observe less tendency for fingering and bypassing and percolation-like patterns are emerging. We thus observe the transition from

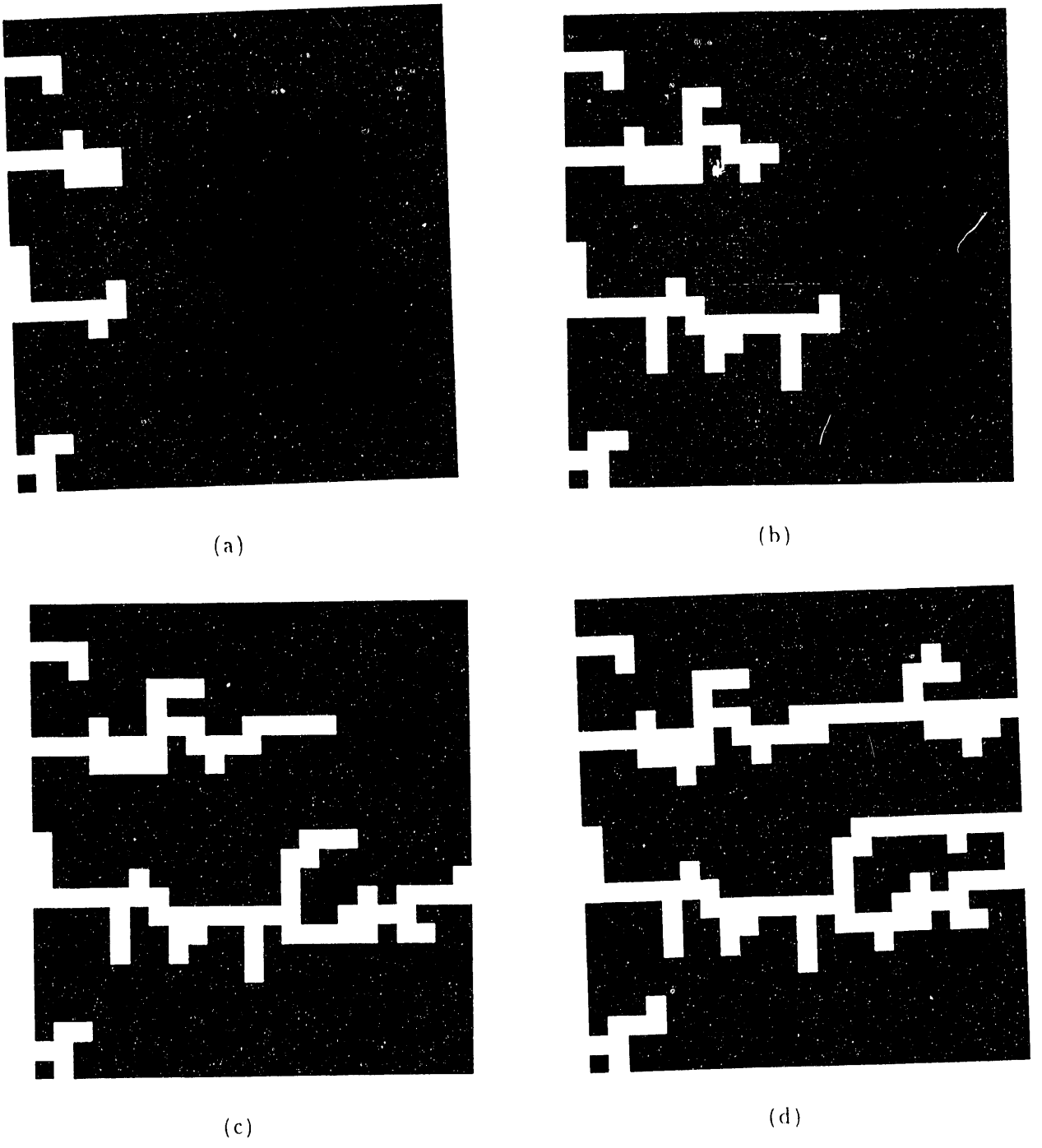

Figure 36: Constant Rate (100 cm/sec) Immiscible Displacement for n=0.35 and K=6.20 $Psec^{n-1}$ (Ca=0.333 and N_p=174.8) at Four Different Time Steps (a) 30 (b) 60 (c) 90 (d) 120.

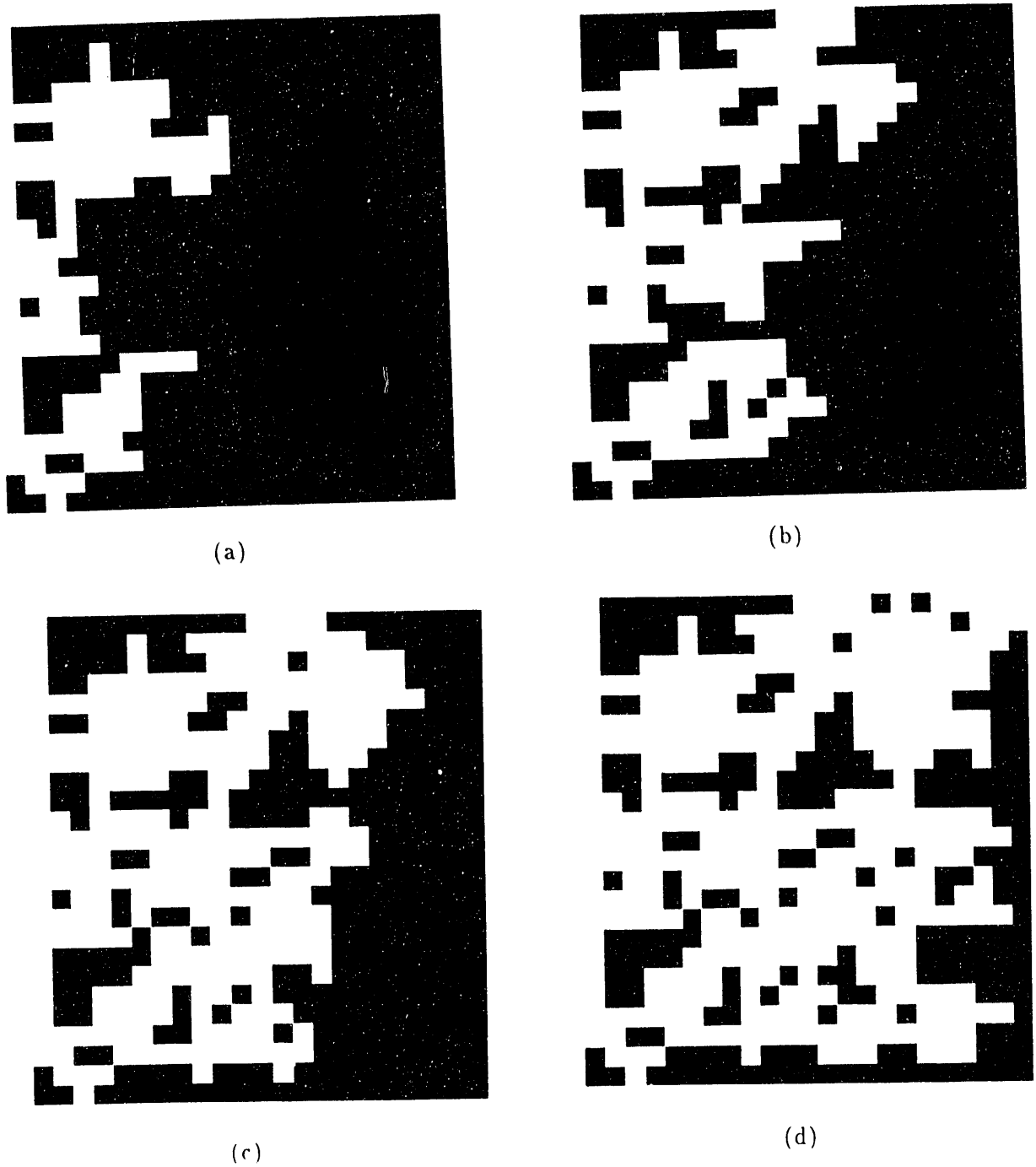

Figure 37: Constant Rate (0.01 cm/sec) Immiscible Displacement for n=0.35 and K=6.20 $Psec^{n-1}$ (Ca=3.33 x 10^{-4} and N_p=0.0174) at Four Different Time Steps (a) 120 (b) 210 (c) 270 (d) 360.

n	$K\ (Psec^{n-1})$
0.75	0.17
0.60	0.43
0.48	1.95
0.35	6.20

Table 1: Power-law Parameters (from [7]).

viscous fingering as the capillary forces increase. Further decrease in the capillary number leads to the capillary fingering domain. Figures 38 and 39 show displacement patterns for the other shear thinning fluid. Although, the tendency for viscous fingering, channeling etc. has decreased, the general trend in the two patterns remains the same. It will be interesting to verify the theoretical stability condition by the numerical simulation of the microdisplacement. Simulation results are shown below for a displacement in the absence of capillary forces.

Figures 40 to 42 show displacement patterns for the shear thinning fluid with power-law parameters $n = 0.35$ and $K = 6.20\ Psec^{n-1}$ at various injection rates. As required by the macroscopic analysis, we have progressively reduced the injection velocity in order to study the transition from instability to stability. Figure 40 shows the displacement patterns for a high injection rate of 1 cm/sec at four different time steps. We observe pronounced viscous fingering with the invading non-Newtonian fluid rapidly trying to break-through. As we decrease the injection velocity to 0.01 cm/sec (Figure 41), the tendency for viscous fingering has disappeared and the interface advances uniformly. Figure 42 represents displacement patterns for the much lower injection velocity of 0.0001 cm/sec. We now observe almost piston-like displacement of the interface and the tendency for viscous fingering no longer exists for such low velocity. The opposite results were obtained for shear thickening fluids with power-law parameters $n = 2.0$ and $K = 0.1\ Psec^{n-1}$ as shown in Figures 43 and 44. Now, macroscopic stability requires high interfacial velocities. Figure 43 shows displacement patterns for an injection velocity of 0.00001 cm/sec. We observe unstable interface and fingering. As we increase the injection rate to 0.01 cm/sec piston-like movement of the interface sets in (Figure 44). Both these results confirm the validity of the macroscopic predictions of Pascal [28].

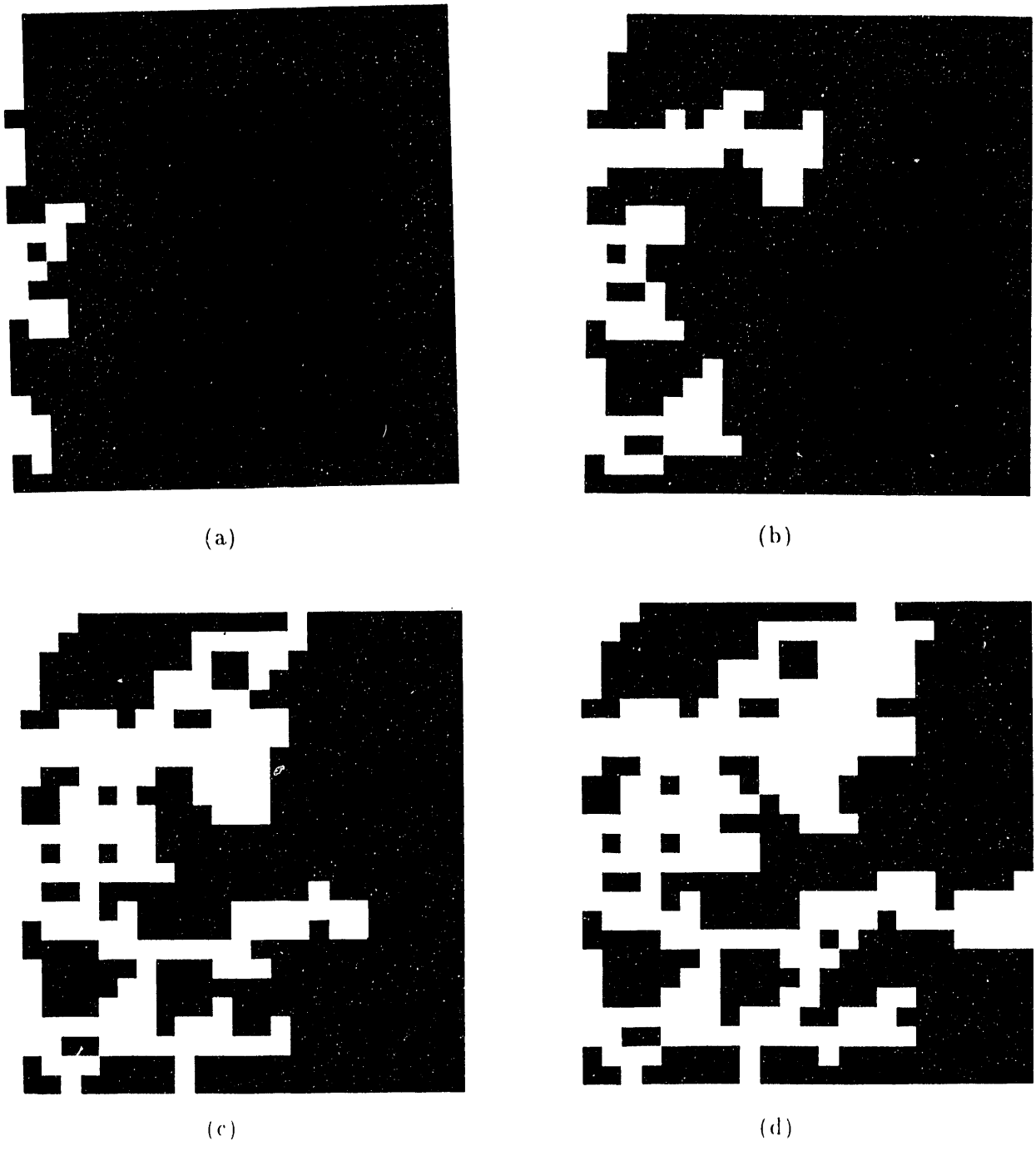

Figure 38: Constant Rate (1 cm/sec) Immisccible Displacement for n=0.6 and K=0.43 $Psec^{n-1}$ (Ca=3.33 $\times$ 10^{-2} and N_p=26) at Four Different Time Steps (a) 30 (b) 90 (c) 180 (d) 240.

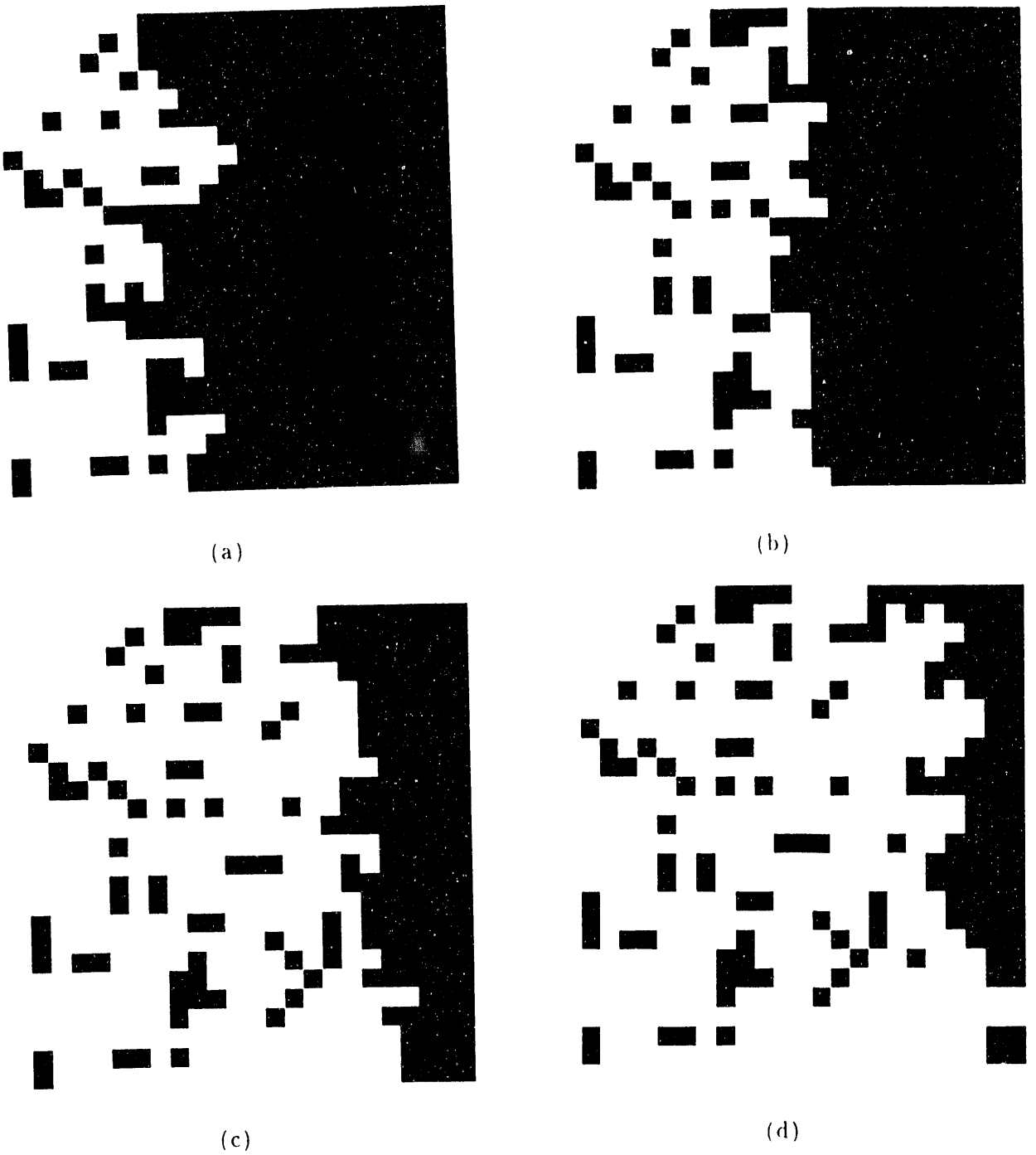

Figure 39: Constant Rate (0.01 cm/sec) Immiscible Displacement for n=0.6 and K=0.43 $Psec^{n-1}$ (Ca=3.33 $\times$ 10^{-4} and N_p=0.26) at Four Different Time Steps (a) 180 (b) 240 (c) 360 (d) 420.

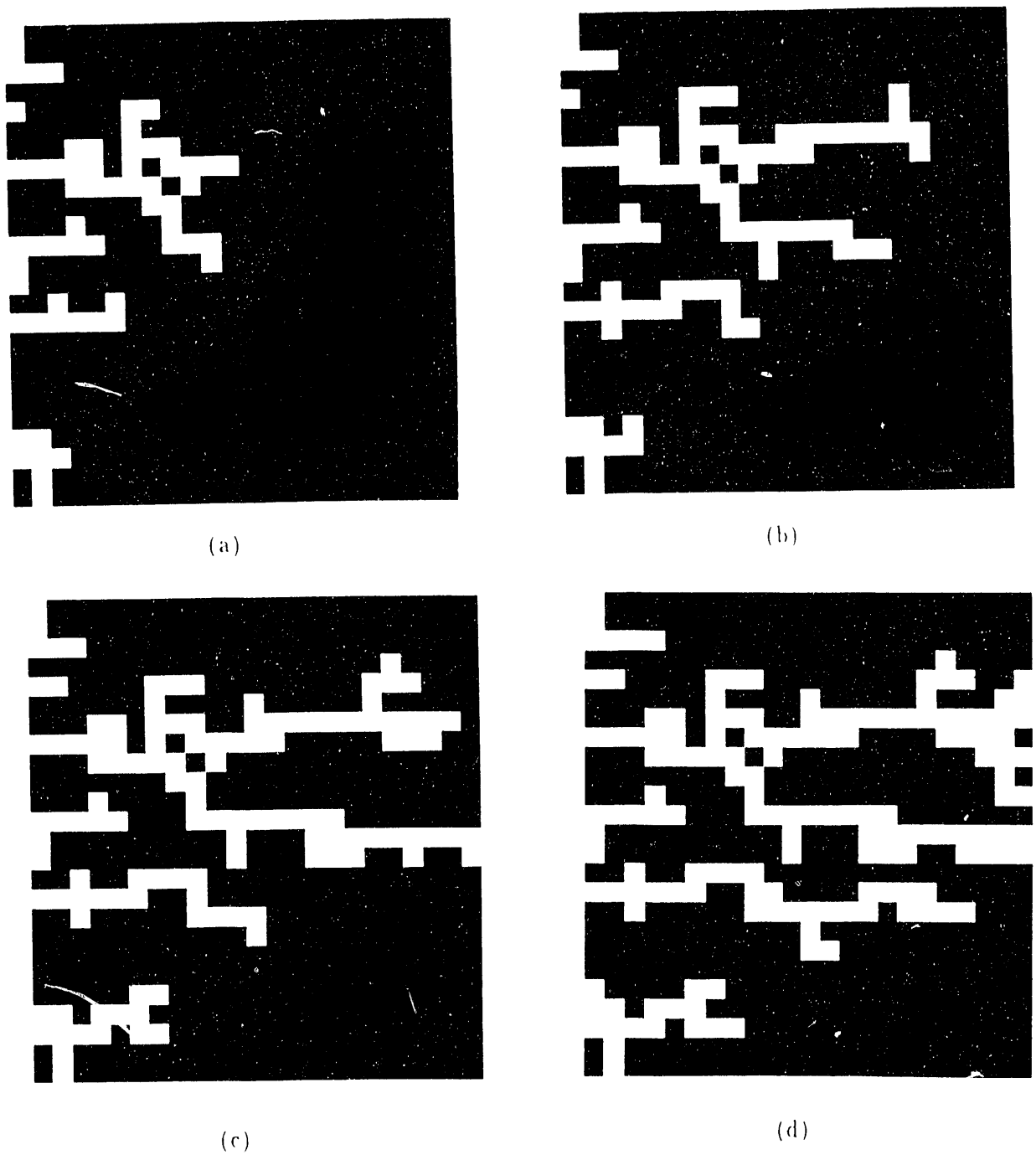

Figure 40: Constant Rate (1 cm/sec) Immiscible Displacement for n=0.35 and K=6.20 $Psec^{n-1}$ in the Absence of Capillary Effect at Four Different Time Steps (a) 60 (b) 90 (c) 120 (d) 150.

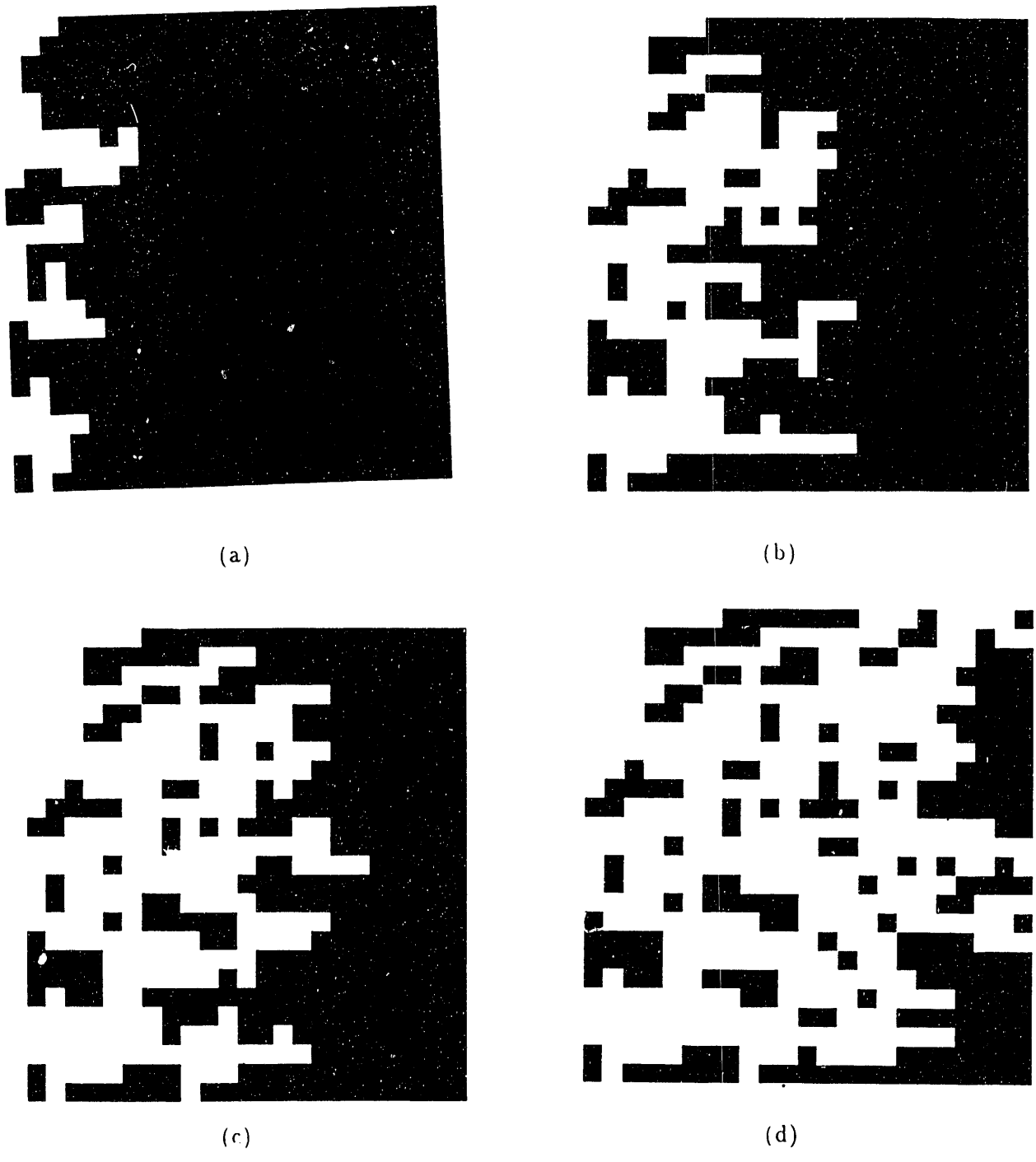

Figure 41: Constant Rate (0.01 cm/sec) Immiscible Displacement for n=0.35 and K=6.20 $Psec^{n-1}$ in the Absence of Capillary Effect at Four Different Time Steps (a) 60 (b) 180 (c) 240 (d) 360.

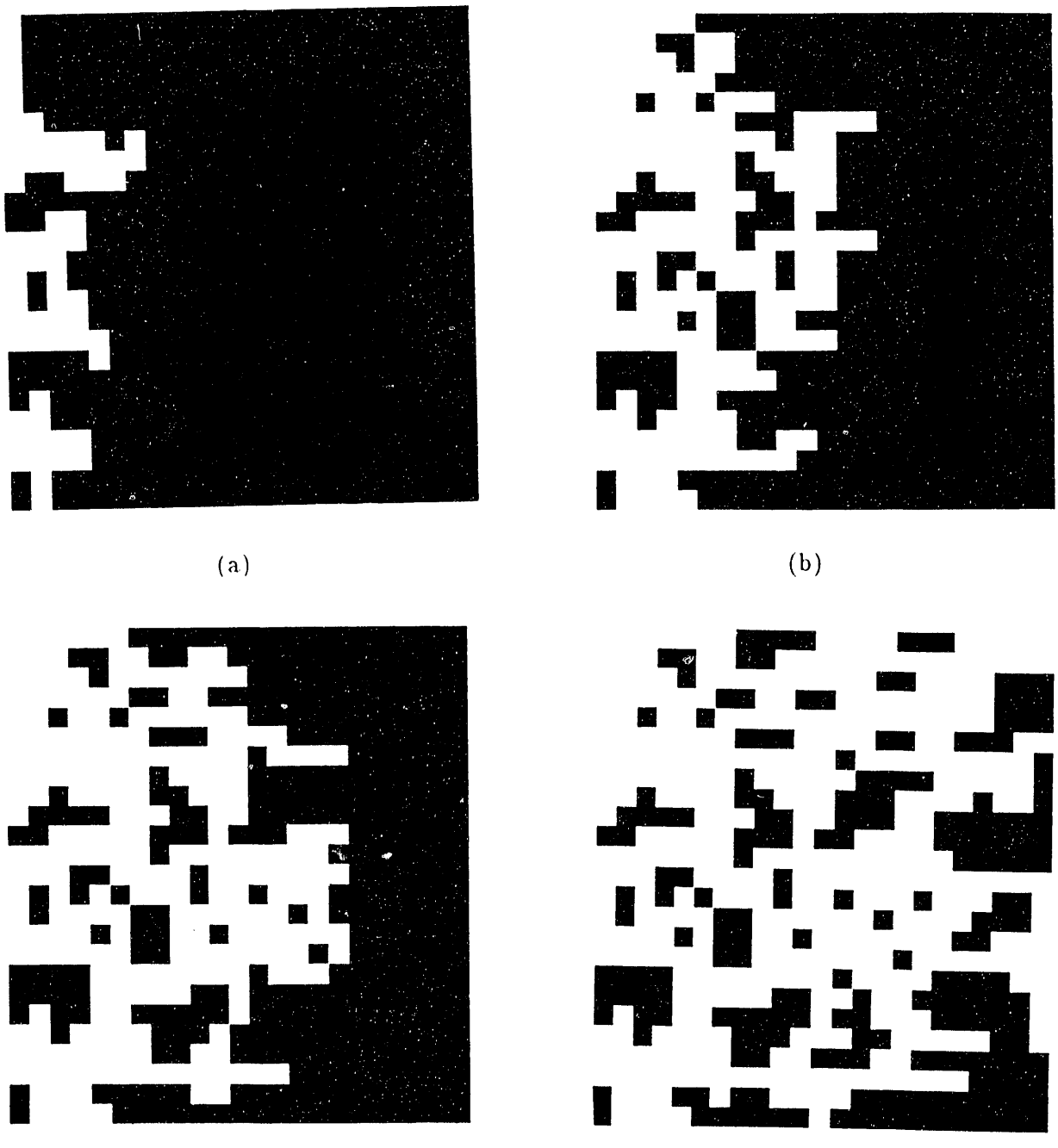

Figure 42: Constant Rate (0.0001 cm/sec) Immiscible Displacement for n=0.35 and K=6.20 $Psec^{n-1}$ in the Absence of Capillary Effect at Four Different Time Steps (a) 60 (b) 180 (c) 240 (d) 360.

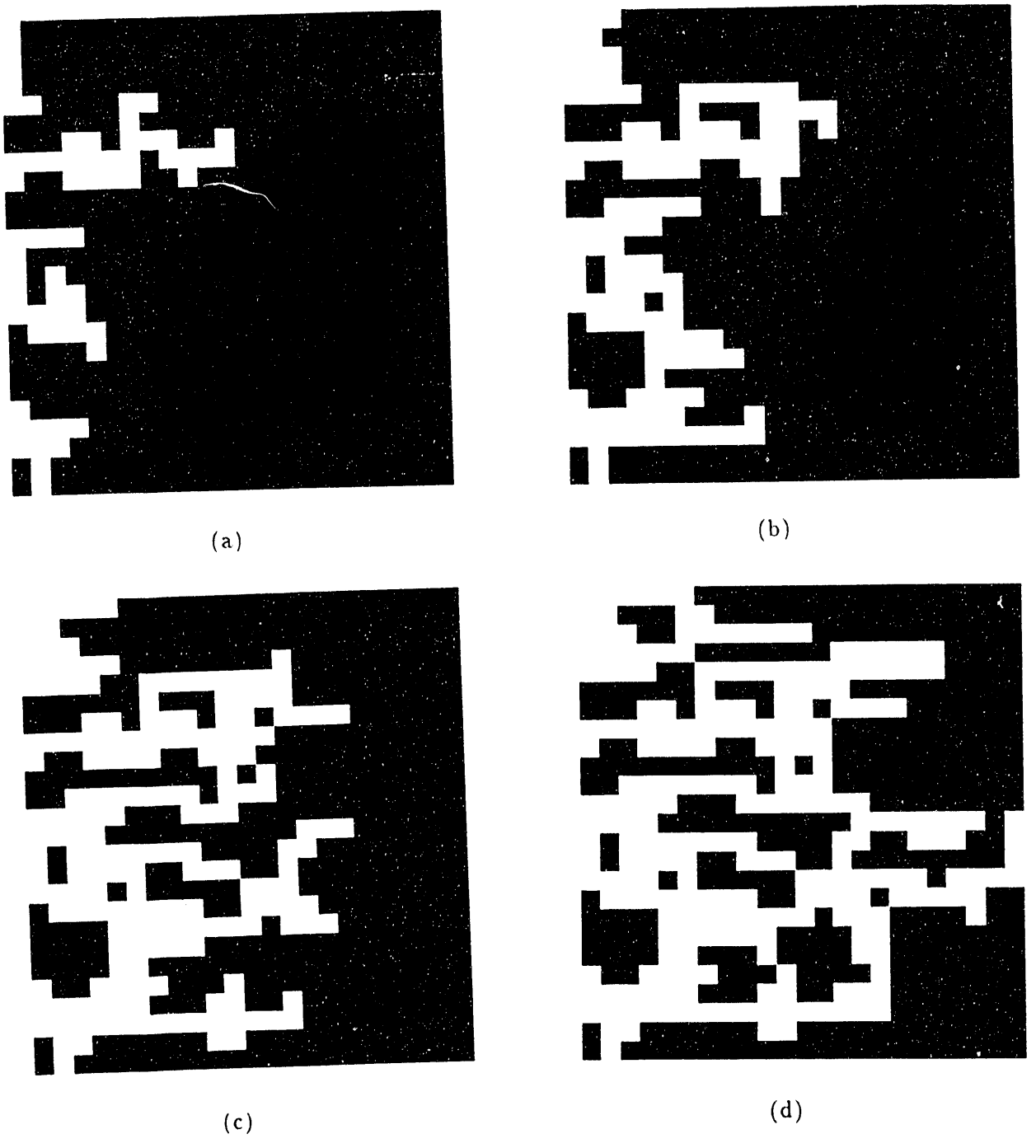

Figure 43: Constant Rate (0.00001 cm/sec) Immiscible Displacement for n=2.0 and K=0.1 $Psec^{n-1}$ in the Absence of Capillary Effect at Four Different Time Steps (a) 60 (b) 120 (c) 180 (d) 240.

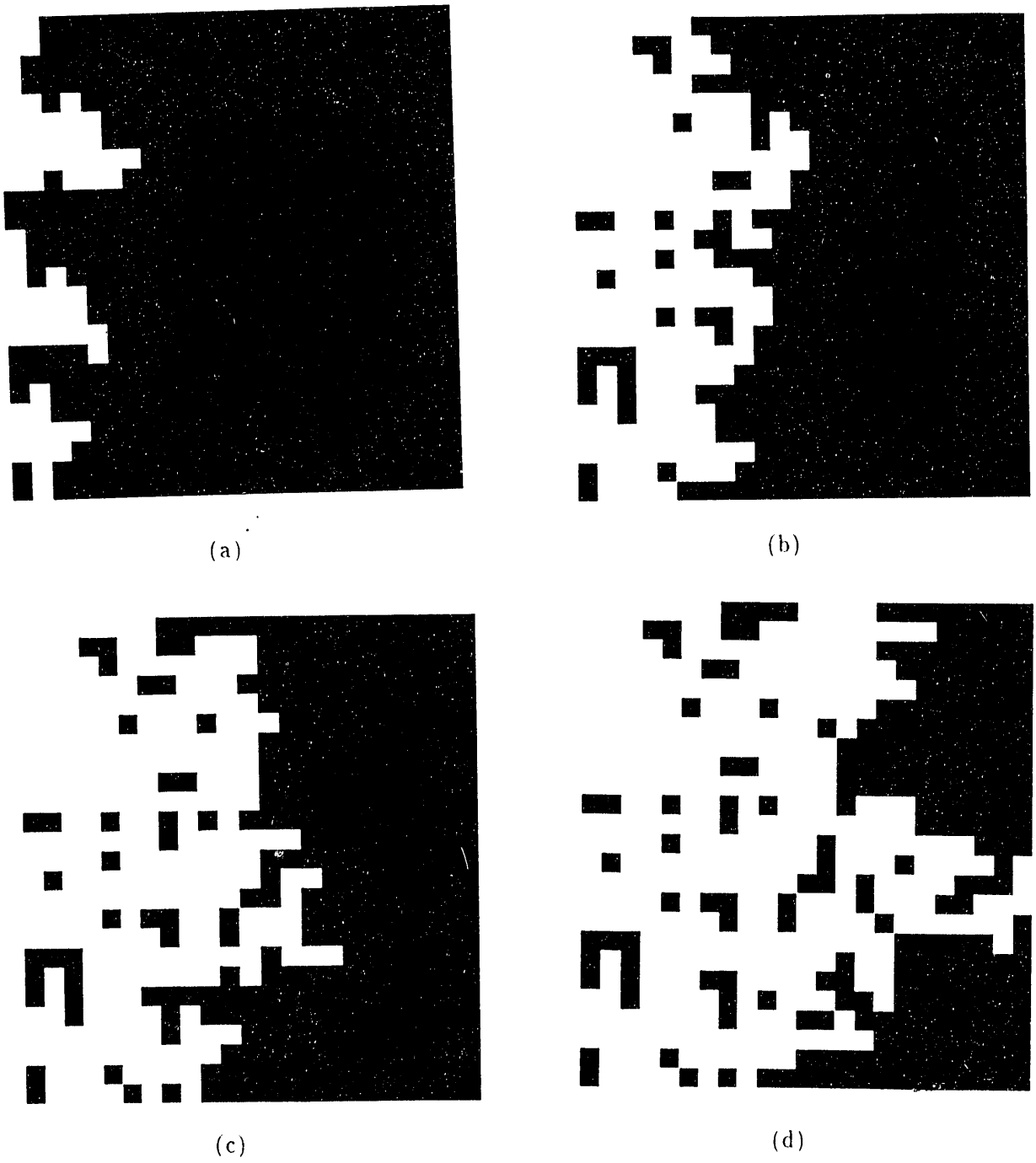

Figure 44: Constant Rate (0.01 cm/sec) Immiscible Displacement for n=2.0 and K=0.1 $Psec^{n-1}$ in the Absence of Capillary Effect at Four Different Time Steps (a) 60 (b) 180 (c) 240 (d) 330.

6 DRAINAGE INVOLVING TWO POWER-LAW FLUIDS

In the previous section, we discussed drainage patterns when the displacing fluid is non-Newtonian but the displaced fluid is Newtonian. It is also important to understand the patterns when both displacing and displaced fluids are of the power-law type [31]. The principle of the simulation is as described previously except that the viscosities of both displacing and displaced fluids are now varying with the shear rate. We shall study the case where the power-law index n is the same for both displacing and displaced fluids, but the consistency index K differs. The two appropriate dimensionless numbers are the modified capillary number Ca and the ratio of consistency indices M, defined as

$$Ca = \frac{K_1 q^n}{R^{n-1}\gamma} \tag{54}$$

and

$$M = (\frac{K_2}{K_1})^{1/n} \tag{55}$$

where K_1 and K_2 denotes the consistency indices for displacing and displaced fluids, respectively, and R is a characteristic radius of the network. The network size was 25 x 25. We carried out a sensitivity analysis for the effect of capillary number (at constant M) and the effect of M (at constant Ca). Simulations were run until a steady state was reached. In all simulations, black denotes pores occupied by the invading fluid. The power-law index n was chosen as 0.6 for the two non-Newtonian fluids.

In the first series, the value of M was set to 14.7. At high flow rates, the patterns are characteristic of viscous fingering (Figures 45), while at low Ca, the displacement patterns is very similar to capillary fingering (Figures 46 and 47). In the second series, M was set equal to 0.07. The resulting flow patterns are shown in Figure 48 for a low capillary number. We can observe a stable displacement as in the Newtonian case when a more-viscous fluid is injected. In all simulations, we observe the transition from one pattern to the other depending on the relative ratio of viscous to capillary effects.

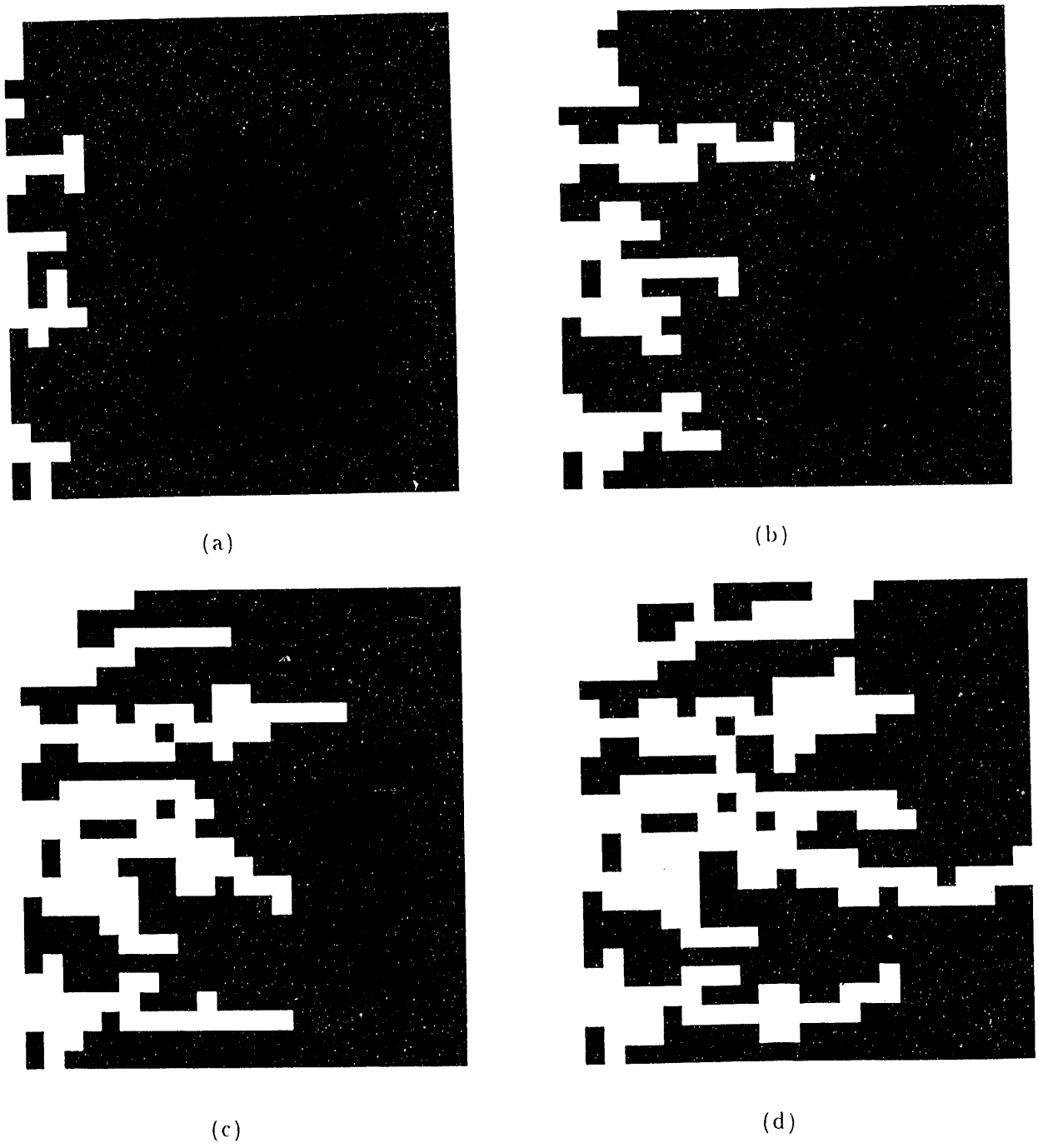

Figure 45: Viscous Fingering at Constant Rate (0.01 cm/sec) Immiscible Displacement for n_1=n_2=0.6 (Ca=0.001 and M=14.7) at Four Different Time Steps (a) 90 (b) 210 (c) 330 (d) 450.

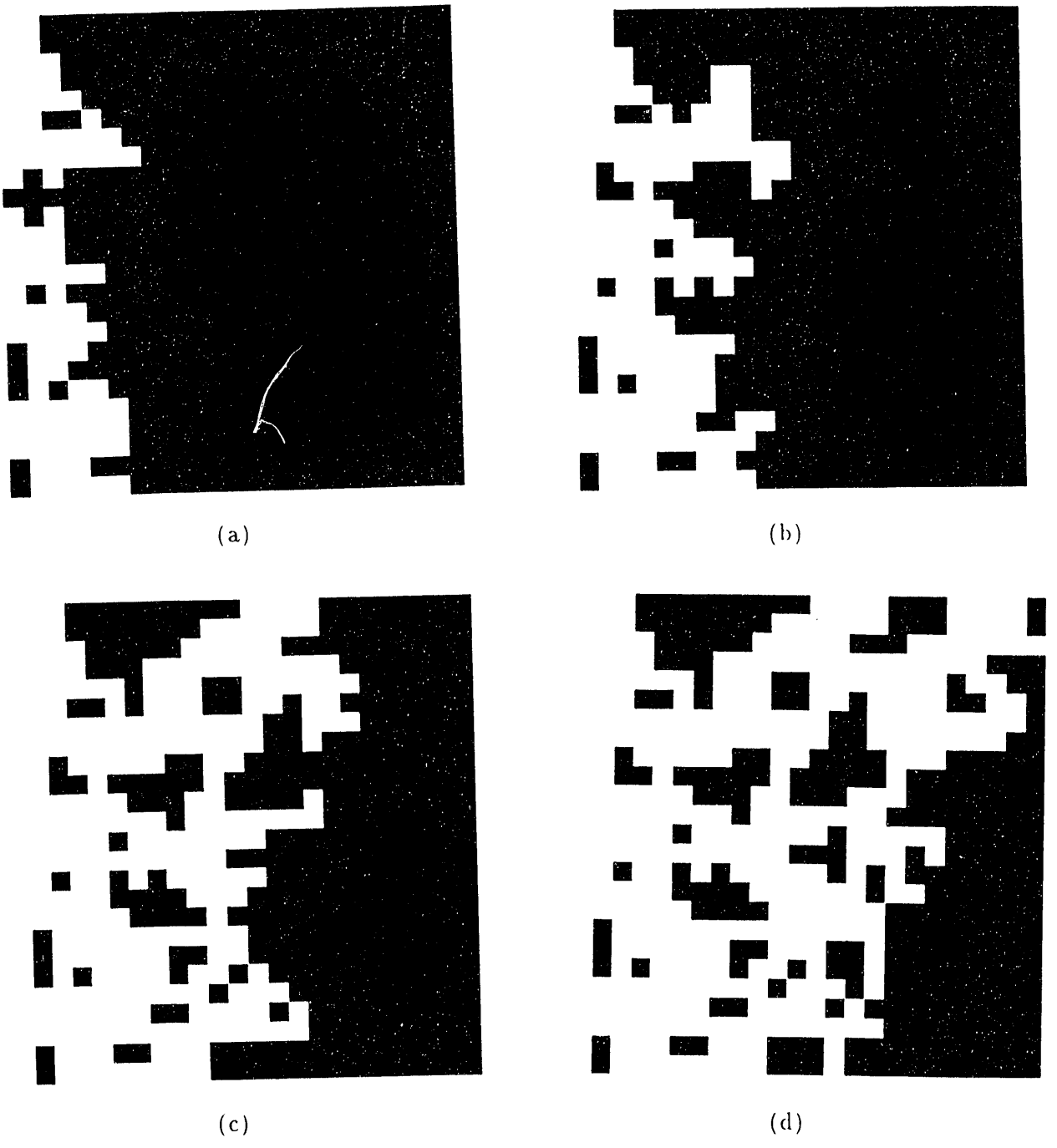

Figure 46: Capillary Fingering at Constant Rate (0.001 cm/sec) Immiscible Displacement for n_1=n_2=0.6 (Ca=8.4 $\times$ 10^{-7} and M=14.7) at Four Different Time Steps (a) 90 (b) 150 (c) 240 (d) 316.

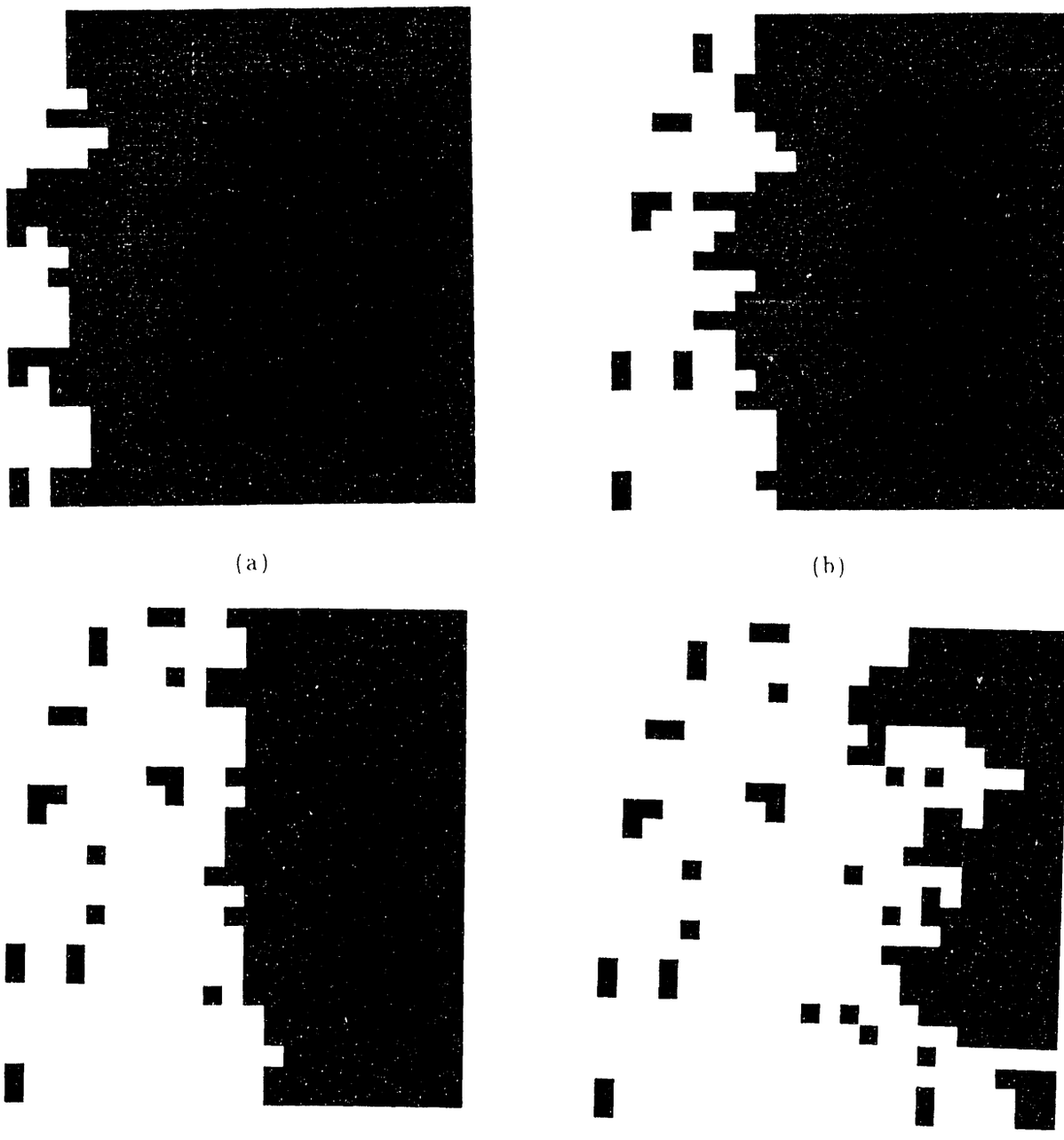

Figure 47: Capillary Fingering at Constant Rate (0.001 cm/sec) Immiscible Displacement for n_1=n_2=0.6 (Ca=4.2 $\times$ 10^{-7} and M=3.2) at Four Different Time Steps (a) 60 (b) 150 (c) 270 (d) 388.

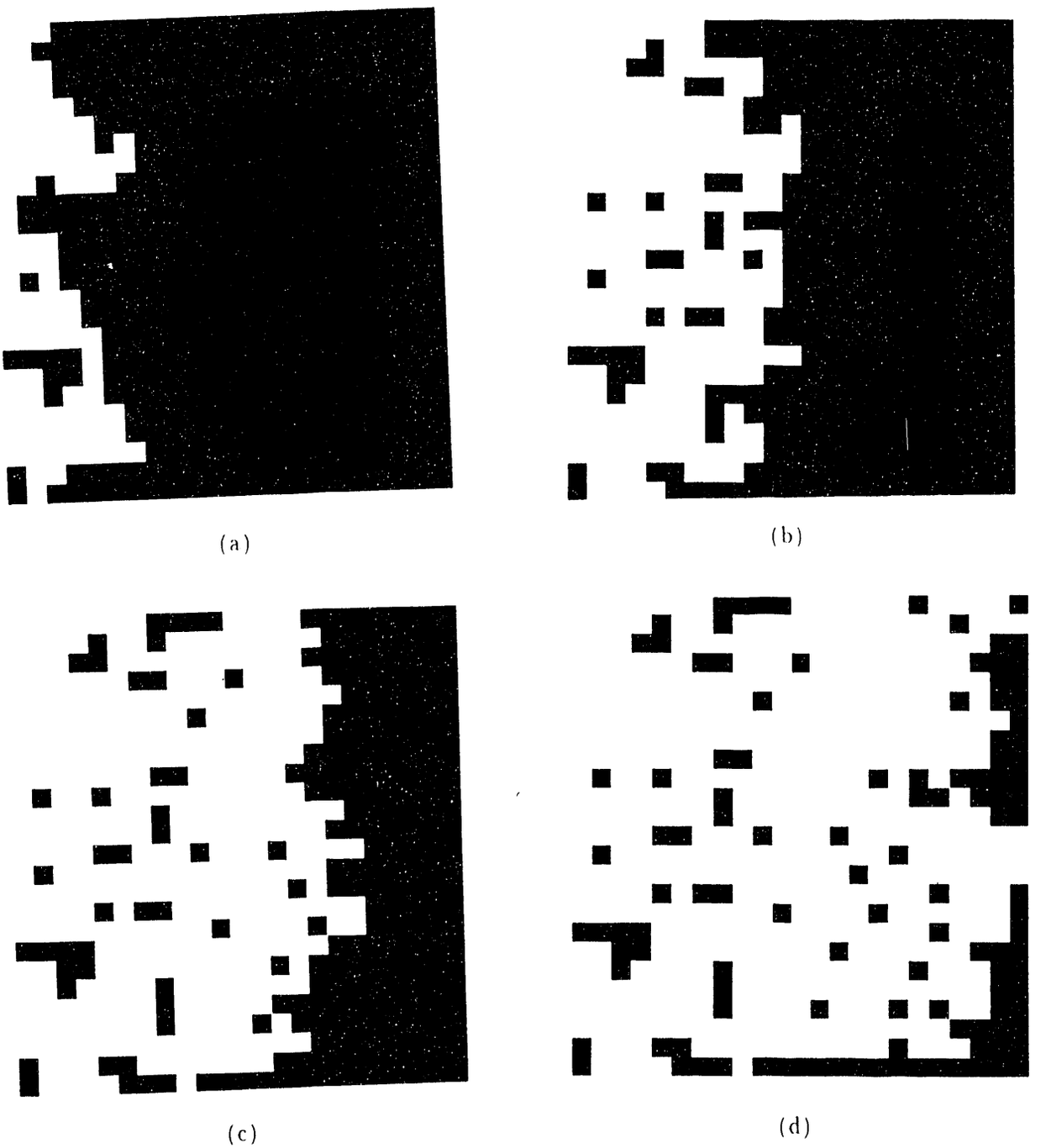

Figure 48: Stable Displacement at Constant Rate (0.001 cm/sec) Immiscible Displacement for $n_1=n_2=0.6$ ($Ca=0.005$ and $M=0.07$) at Four Different Time Steps (a) 30 (b) 90 (c) 150 (d) 210.

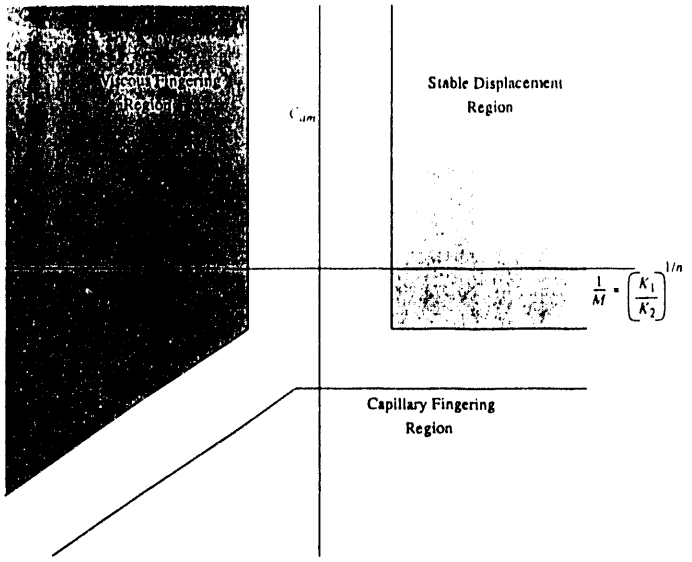

Figure 49: Schematic Phase Diagram for Immiscible Displacement for Non-Newtonian Fluids.

6.1 DOMAIN BOUNDARIES

Comparison of the above results for n=0.6 with other simulations for n=0.4 indicated that all the three displacement domains are observed, although the boundaries of the domains change depending on the power-law index n. The three basic domains can be mapped on a plane with axes Ca and M as shown in Figure 49. A detailed discussion of these three domains for Newtonian fluids was presented by Lenormand [25]. Here, we shall extend his analysis to power-law fluids. The principle of the calculation is the same as in the Newtonian case [25]. We define the limit Ca^* or M^* of each domain such that

$$|S(M^*) - S(plateau)| = \epsilon \tag{56}$$

where S is the saturation at breakthrough and ϵ is a small constant. The analysis proceeds as follows:

Consider a pore network of size $L \times L$ of bond length equal to a. The bonds are uniformly distributed. For single-phase flow of a power-law fluid, the pressure gradient $\Delta P/L$ across the network is expressed in terms of the volumetric flow rate Q, the permeability k, the cross-sectional

area A and the consistency index of invading fluid K_2

$$\frac{\Delta P}{L} = \frac{K_2 Q^n}{kA} \tag{57}$$

The mean conductance g_o for a power-law fluid in a single capillary is

$$g_o = \frac{\pi^n}{2K_2 a} R_o^{3n+1} (\frac{n}{3n+1})^n \tag{58}$$

Hence,

$$k = \frac{\pi^n}{2a^2} R_o^{3n+1} (\frac{n}{3n+1})^n \tag{59}$$

Following the arguments of Lenormand [25] and based on percolation theory we can express

$$L/a \propto (p_c - p^*)^{-\nu} \tag{60}$$

$$N_b/L^2 \propto (p_c - p^*)^{\beta} \tag{61}$$

and

$$G/g_o \propto (p_c - p^*)^{t_n} \tag{62}$$

where p_c and p^* denote the percolation threshold for a network of size L and for an infinite network, respectively. Here, exponent t_n is also dependent on the power-law index n. Now, due to viscous effects, the pressure will increase at the entrance. When we inject the fluid with the higher consistency index, we shall have

$$\Delta P = \frac{Q^n}{G} \tag{63}$$

The corresponding variation of size of the accessible throats is

$$\frac{\Delta R}{R_o} = R_o \Delta P/\gamma \tag{64}$$

while the variation Δp of the fraction of accessible bonds is

$$\Delta p = \Delta R/2\sigma R_o \tag{65}$$

where σ is the standard deviation for the distribution of bonds. The corresponding variation of bonds in the cluster is obtained by taking the derivative of equation (61)

$$\Delta N/L^2 \propto (p_c - p^*)^{\beta-1}\Delta p \tag{66}$$

Substituting the values of Δp, ΔR and g_o from equations (61), (64) and (62) respectively, we get

$$\frac{\Delta N}{L^2} \propto (\frac{L}{a})^{(1+t_n-\beta)/\nu}\frac{aK_1Q^n}{R_o^{3n}\sigma\gamma} \tag{67}$$

To obtain the limiting value Ca^* on the boundary we equate the relative variation $\Delta N/N_b$ in the number of bonds in the percolation cluster to ϵ

$$(\frac{L}{a})^{(1+t_n+n\nu)/\nu}\frac{a^{2n+1}}{R_o^{3n}}\frac{R^{n-1}Ca^*}{\sigma} = \epsilon \tag{68}$$

Thus,

$$Ca^* = \frac{A\epsilon\sigma}{R^{n-1}}(\frac{L}{a})^{(1+t_n+n\nu)/\nu}\frac{R_o^{3n}}{a^{2n+1}} \tag{69}$$

where A is a prefactor and can be evaluated from numerical simulation for a particular value of power-law index.

When we inject the power-law fluid with a lower consistency index, the fraction of accessible channels decreases by a value of Δp due to fingering. The decrease in pressure is given from equation (57) by assuming that the displaced fluid flows in the entire network [25]

$$\Delta P = \frac{K_2Q^nL}{kaL} \tag{70}$$

Following the same approach as before, we obtain the corresponding variation of bonds in the network as

$$\frac{\Delta N}{L^2} \propto \frac{(p_c - p^*)^{\beta-1}aK_2Q^n}{R_o^{3n}\sigma\gamma} \tag{71}$$

or, after substitution,

$$\frac{\Delta N}{L^2} \propto (\frac{L}{a})^{(1-\beta)/\gamma} \frac{L^n}{a^n} \frac{a^{2n+1}}{R_o^{3n}\sigma} CaM^n R^{n-1} \tag{72}$$

The relative variation $\Delta N/N_b$ of the number of bonds in the percolation cluster is given by

$$\frac{\Delta N}{N_b} = (\frac{L}{a})^{(1+\nu n)/\nu} \frac{a^{2n+1} R^{n-1} M^n}{R_o^{3n}\sigma} Ca^* = \epsilon \tag{73}$$

and, finally

$$Ca^* = \frac{B\epsilon\sigma(\frac{L}{a})^{-(1+\nu n)/\nu}}{R^{n-1}} \frac{R_o^{3n}}{a^{2n+1}M^n} \tag{74}$$

The value of the prefactor B can be estimated from simulation results for specific values of the power-law index.

We next derive boundary equations pertaining to the viscous and capillary limits for the viscous fingering domain. For the viscous limit we obtain

$$M^* = \epsilon(\frac{a}{L})^{1/n} \tag{75}$$

while for the capillary limit we get

$$Ca^* = \frac{C\epsilon\sigma(\frac{a}{L})^n}{R^{n-1}} \frac{R_o^{3n}}{a^{2n+1}M^n} \tag{76}$$

where C is a prefactor to be determined from simulation results.

Finally, the boundaries for the stable displacement are obtained: For the capillary limit we have

$$Ca^* = D\epsilon\sigma \frac{R_o^{3n}}{a^{2+n}L^{n-1}r^{n-1}} \tag{77}$$

while for the viscous limit the simple result is found

$$M^* = E/\epsilon \tag{78}$$

where D and E are the prefactors to be determined from simulation.

7 CONCLUSIONS

In this report we described our ongoing research related to the flow of non-Newtonian fluids in porous media. Most of the work presented pertained to power-law fluids in pore networks, where extensional flow effects were neglected. Extension of the research to cover more general viscoelastic fluids is currently under consideration. For power-law fluids we considered the comparison of the numerical simulation results with previous theoretical expressions based on EMT and CPA. Except for very small values of n, the latter was found to be in excellent agreement with the simulations pointing out to the usefulness of CPA-derived estimates for power-law fluid flow in porous media. Numerical simulation of the flow of Bingham plastics, taken to represent the behavior of some heavy oils, showed the existence of a macroscopic yield stress for the onset of flow. This behavior resembled somewhat that of power-law fluids at small values of the exponent n. We subsequently described simulation for the displacement (drainage) of one fluid by another of different power-law indices. Displacement patterns similar to the Newtonian case, namely percolation, viscous fingering and compact displacement were found. For the case of fluids of equal power-law indices, but of different consistency indices, we were able to classify the patterns extending Lenormand's phase diagram to power-law fluids.

References

[1] V. Ambegaokar, B. I. Halperin, and J. S. Langer. *Physical Review B*, 4, No. 6:2612, 1971.

[2] D.M. Binding and K. Walters. *J. of Non-Newtonian Fluid Mechanics*, 30:233, 1988.

[3] R.B. Bird, Steward W.E., and Lightfoot E.N. *Transport Phenomena.* John Wiley and Sons, New York, 1960,1990.

[4] R. Blumenfeld and A. Aharony. *J. Phys.A:Math. Gen.*, 18:L443, 1985.

[5] R. Blumenfeld, Meir Y., Harris B., and A. Aharony. *J. Phys.A:Math. Gen.*, 19:L791, 1986.

[6] D. V. Boger. *Annual Review Fluid Mech.*, 19:157, 1987.

[7] W. J. Cannella and C. Huh. *Society of Petroleum Engineers*, 63rd Annual SPE Fall meeting:353, 1988.

[8] P. J. Carreau. *Trans. Soc.*, 16:99, 1972.

[9] G. Chauveteau. *Paper SPE 10060, Presented at 56th Annual Fall Conf. of SPE*, San Antonio, TX, 1981.

[10] R. H. Christopher and S. Middleman. *Ind. Eng. Chem. Funds.*, 4:422, 1965.

[11] Y. Cohen and F. R. Christ. *SPERE*, March:113, 1986.

[12] R. E. Collins. *Flow of Fluids Through Porous Materials.* The Petroleum Publishing Company, Tulsa, 1976.

[13] G. Dagan. *Flow and Transport in Porous Media.* Springer-Verlag, 1989.

[14] J. L. Duda, S. A. Hong, and E. E. Klaus. *Ind. Eng. Chem. Funds.*, 22:299, 1983.

[15] F. Durst. *J. of Non-Newtonian Fluid Mechanics*, 22:169, 1987.

[16] R.E. Evans and K. Walter. *J. of Non-Newtonian Fluid Mechanics*, 20:11, 1986.

[17] M. Greaves and K. Patel. *Chem. Eng. Res. Des.*, 63:199, 1985.

[18] G. J. Hirasaki and G. A. Pope. *SPE Journal*, August:337, 1974.

[19] D.M. Jones and K. Walter. *Rheological Acta*, 28:482, 1989.

[20] D.M. Jones, K. Walter, and Williams P.R. *Rheological Acta*, 26:20, 1987.

[21] A. J. Kart and A. H. Thompson. *J. of Geophysical Research*, 92:599, 1987.

[22] X. Kong, M. Haghighi, and Y. C. Yortsos. *Fuel*, 71:1462, 1992.

[23] J. Koplik. *J. Phys. C*, 14:4821, 1981.

[24] J. Koplik. *J. Fluid Mech.*, 119:219, 1987.

[25] R. Lenormand. *Proc. R. Soc. Lond.*, A423:159, 1989.

[26] R. Lenormand, E. Touboul, and C. Zarcone. *J. Fluid Mech.*, 189:165, 1988.

[27] R. J. Marshal and A. B. Metzner. *Ind. Eng. Chem. Funds.*, 6:393, 1967.

[28] H. Pascal. *Acta Mechanica*, 58:81, 1986.

[29] H. Pascal. *Int. J. Engng. Sci.*, 24, No 9:1465, 1986.

[30] H. Pascal. *Canadian Journal of Chemical Engg.*, 64:375, 1986.

[31] H. Pascal. *J. of Colloidal and Interface Science*, 123, No 1:14, 1988.

[32] L. Paterson. *Phys. Rev. Lett.*, 52:1621, 1984.

[33] W. R. Rossen, Z. H. Zhou, and C. K. Mamun. *Society of Petroleum Engineers*, 66th Annual SPE meeting:1, 1991.

[34] T. J. Sadowski. *Trans. Soc. Rheol.*, 9, No 2:251, 1965.

[35] T. J. Sadowski and R. B. Bird. *Trans. Soc. Rheol.*, 9, No 2:243, 1965.

[36] M. Salman. *Ph.D. Thesis, University of Southern California*, 1989.

[37] M. Salman, S. Baghdikian, L.L. Handy, and Y.C. Yortsos. submitted. *SPERE*, 1989.

[38] J. G. Savins. *Industrial and Engineering Chemisrty*, 61:19, 1969.

[39] J. G. Savins and C. A. Dimon. *J. of Petroleum Science and Engineering*, 1:163, 1987.

[40] F. N. Schneider and W. W. Owens. *Paper SPE 9408, Presented at the 55th Annual Meeting*, Dallas, Sep. 20-24, 1980.

[41] C. B. Shah and Y.C. Yortsos. *Modification Of Chemical and Physical Factors in Steamflood to increase Heavy Oil Recovery-Chapter 7.* Annual Report, DOE, April 1992.

[42] R. E. Sheffield and A. B. Metzner. *AICHE Journal*, 22:736, 1979.

[43] J. C. Slattery. *AICHE Journal*, 14, No 1:50, 1968.

[44] K. S. Sorbie, P. J. Clifford, and E. R. W. Jones. *J. of Colloidal and Interface Science*, 130:508, 1989.

[45] K.S. Sorbie. *Paper SPE 19651 presented at the 64th SPE Annual Fall Meeting*, San Antonio, October 8-11, 1989.

[46] K.S. Sorbie. *Lecture Series 1990-01 on Modelling and Applications of Transport Phenomena in Porous Media, Van Karman Institute, Brussels, Belgium*, Feb. 05-09, 1990.

[47] D. Teeuw and F. Hesselink. *Paper SPE 8982 presented at the 5th SPE International Symposium on Oilfield and Geothermal Chemistry*, Stanford, May 28-30, 1980.

[48] S. Whitaker. *Industrial and Engineering Chemistry*, 61, No 12:14, 1969.

[49] D. Wilkinson and J. F. Willemsen. *J. Phys.A*, 16:3365, 1983.

[50] G. P. Willhite and J. T. Uhl. *Proceedings, ACS Division of PMSE, Fall Meeting*, Anaheim, California, Sep., 1986.

[51] Y. S. Wu, K. Pruess, and P. A. Witherspoon. *SPERE*, August:369, 1992.

[52] Y-S. Wu, K. Pruess, and P.A. Witherspoon. *Society of Petroleum Engineers*, 60th California Regional Meeting:339, 1990.

[53] Y.C. Yortsos. *Modification Of Chemical and Physical Factors in Steamflood to increase Heavy Oil Recovery-Chapter 7.* Annual Report, DOE, April 1991.

[54] A. Zaitoun and G. Chauveteau. *Proceedings of European Symposium on EOR*, Bournemouth, England, Sep. 21-23, 1981.

APPENDIX A SOLUTION METHOD

Following the notation of Figure 50, the mass balance at the node (i, j) is

$$g_1(P_{i,j+1} - P_{i,j})^{1/n} + g_2(P_{i+1,j} - P_{i,j})^{1/n} + g_3(P_{i,j-1} - P_{i,j})^{1/n} + g_4(P_{i-1,j} - P_{i,j})^{1/n} = 0 \quad \text{(A.1)}$$

where g denotes conductance and P denotes node pressure (Figure 50). There are $N \times M$ such equations where N and M are the number of nodes on the horizontal and lateral sides of the network. Equation (A.1) is nonlinear and is solved by a successive relaxation iterative method. We first rewrite

$$P_{ij} = \frac{\frac{g_1 P_{i,j+1}}{U_1} + \frac{g_2 P_{i+1,j}}{U_2} + \frac{g_3 P_{i,j-1}}{U_3} + \frac{g_4 P_{i-1,j}}{U_4}}{\frac{g_1}{U_1} + \frac{g_2}{U_2} + \frac{g_3}{U_3} + \frac{g_4}{U_4} +} \quad \text{(A.2)}$$

and subsequetly apply successive relaxation as follows

$$P_{ij} = \omega\left(\frac{\frac{g_1 P_{i,j+1}}{U_1} + \frac{g_2 P_{i+1,j}}{U_2} + \frac{g_3 P_{i,j-1}}{U_3} + \frac{g_4 P_{i-1,j}}{U_4}}{\frac{g_1}{U_1} + \frac{g_2}{U_2} + \frac{g_3}{U_3} + \frac{g_4}{U_4} +}\right) + (1 - \omega)F \quad \text{(A.3)}$$

where ω is a under-relaxation parameter, F is the value of P_{ij} from the previous iteration and

$$U_1 = (|P_{i,j+1} - F|)^{\frac{n-1}{n}} \quad \text{(A.4)}$$

$$U_2 = (|P_{i+1,j} - F|)^{\frac{n-1}{n}} \quad \text{(A.5)}$$

$$U_3 = (|P_{i,j-1} - F|)^{\frac{n-1}{n}} \quad \text{(A.6)}$$

$$U_4 = (|P_{i-1,j} - F|)^{\frac{n-1}{n}} \quad \text{(A.7)}$$

The point iteration method was found to lead to good results for all the values of power-law index studied in this report. A good initial guess for each pressure in the network will help in achieving faster convergence for the set of $N \times M$ nonlinear equations.

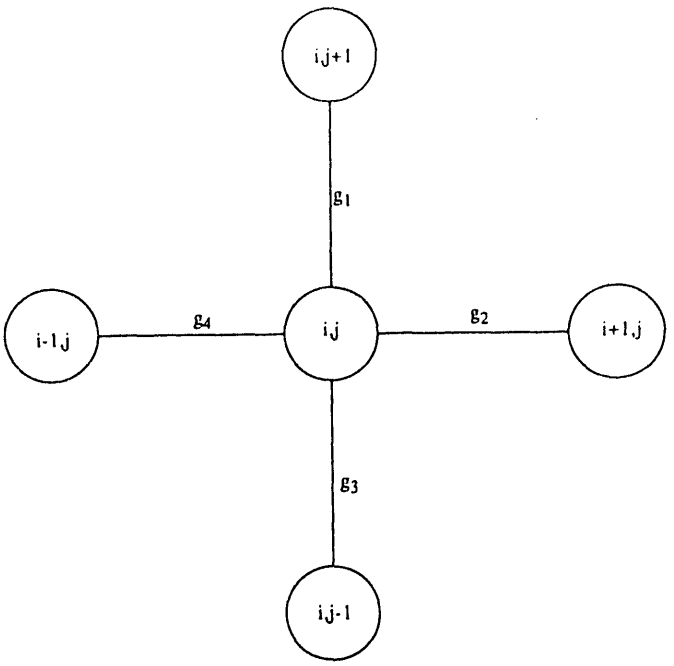

Figure 50: Network Schematic.

APPENDIX B DIMENSIONAL NOTATION

If we define inlet and outlet pressures for the network as P_{in} and P_{out}, respectively, the dimensionless pressure π_{ij} is

$$\pi_{ij} = \frac{P_{ij} - Pout}{P_{in} - P_{out}} \tag{B.1}$$

We next define dimensionless quantities as follows $R_{ij} = \rho_{ij} R^*$ and $g_{ij} = \sigma_{ij} g_n{}^*$, where $*$ denotes a characteristic quantity. For power-law fluids, we have

$$g_n^* = \pi R^{* \frac{3n+1}{n}} (\frac{n}{3n+1})(\frac{1}{2KL})^{1/n} \tag{B.2}$$

and

$$\sigma_{ij} = \rho_{ij}{}^{\frac{3n+1}{n}} \tag{B.3}$$

The capillary condition for the advancement of menisci in drainage is

$$P_i - P_j \geq P_c \tag{B.4}$$

which in view of the above becomes

$$\pi_i - \pi_j \geq \frac{2\gamma}{\rho_{ij} R^* \Delta P} \tag{B.5}$$

The conventional capillary number based on the flow of Newtonian fluid in the network is

$$N_{caP} = \frac{Q}{\mu} A\gamma \tag{B.6}$$

where, N_{caP} is a capillary number based on total pressure drop across the network of size $N \times M$. In expression (B.6), we can substitute Q from Darcy's law for Newtonian flow in porous media and assuming a permeability k dependence as R^{*2}, we obtain

$$N_{caP} = \frac{R^{*2} \Delta P}{NL\gamma} \tag{B.7}$$

Based on these, we can express the displacement condition as

$$\pi_i - \pi_j \geq \frac{2R^*}{\rho_{ij} N L N_{caP}} \tag{B.8}$$

Finally, we can define the dimensionless flow rate $Q_{D_{ij}}$ as

$$Q_{ij} = Q_{D_{ij}} Q^* \tag{B.9}$$

where

$$Q^* = g_1{}^* \Delta P^{1/n} \tag{B.10}$$

depending upon the type of the fluid present in the bonds of the network. The dimensionless flow through the network is

$$Q_{D_n} = \sum_{inj} \sigma_{ij} (\pi_i - \pi_j)^{1/n} \tag{B.11}$$

or

$$Q_D = \sum_{out} \sigma_{ij} (\pi_i - \pi_j) \tag{B.12}$$

Based on the above, the capillary number Ca is

$$Ca = \frac{Q_D N N_{caP}}{8M} \tag{B.13}$$

END

DATE
FILMED
4/28/93